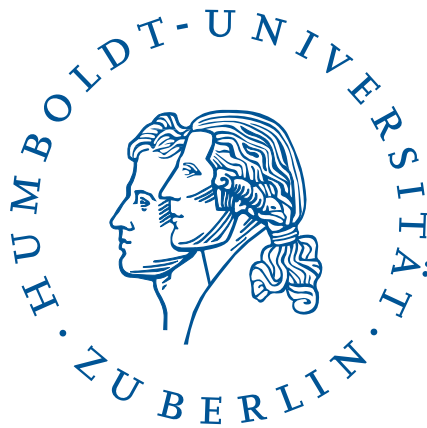


Structural stability and electronic properties of the
thermoelectric clathrates $\text{Ba}_8\text{Al}_x\text{Si}_{46-x}$ and
 $\text{Sr}_8\text{Al}_x\text{Si}_{46-x}$

MASTERARBEIT

zur Erlangung des akademischen Grades
Master of Science
(M. Sc.)
im Fach Physik



eingereicht an der
Mathematisch-Naturwissenschaftlichen Fakultät I
Institut für Physik
Humboldt-Universität zu Berlin

von
Frau Maria Troppenz
geboren am 24.11.1989 in Berlin

Gutachter:

1. *Prof. Dr. Dr. h.c. Claudia Draxl*
2. *Prof. Dr. Saenz*

Betreut von:

1. *Prof. Dr. Dr. h.c. Claudia Draxl*
2. *Dr. Santiago Rigamonti*

eingereicht am: 15. Dezember 2015

Abstract

Clathrate compounds are promising candidates for high-efficiency thermoelectric applications. Their cage-like structure containing guest atoms allows for exploiting the idea of the phonon-glass electron-crystal and reaching a large figure of merit. In this work, the structural stability and electronic properties of $\text{Ba}_8\text{Al}_x\text{Si}_{46-x}$ and $\text{Sr}_8\text{Al}_x\text{Si}_{46-x}$ in the compositional range $6 \leq x \leq 16$ are studied. Optimal electronic transport properties are expected close to the Zintl composition ($x=16$). Due to the large number of substitutional configurations we make use of a special iterative cluster expansion (CE) approach to find the ground state configurations. For both clathrate compounds, a CE with a predictive power of 1-2 meV/atom is obtained. Regarding the structural properties, a linear increase of the lattice constant with the number of Al substituents is obtained (0.019 Å per Al addition) confirming experimental observations (0.02 Å). Furthermore, the calculated bond distances between high-symmetry sites agree well with experiment for the full compositional range. The substitutional configurations present an order-disorder transition around 600-900 K. In addition, the substitutional ordering at the Zintl composition leads to a metal-semiconductor transition, which makes these compounds promising for technological applications.

Contents

1	Introduction	1
2	Type-I clathrates	3
2.1	Clathrate structure	3
2.2	$\text{Ba}_8\text{Al}_x\text{Si}_{46-x}$ and $\text{Sr}_8\text{Al}_x\text{Si}_{46-x}$	4
2.3	Combinatorial explosion	5
3	Cluster-expansion approach	7
3.1	Formalism	7
3.2	Search for a CE with high validity	8
3.3	Realization of the cluster expansion	10
3.3.1	Common cluster expansion codes	10
3.3.2	CELL - cluster expansion with large parent cells	12
4	<i>Ab-initio</i> calculations with DFT	14
4.1	Kohn-Sham equations	14
4.2	Linearized augmented plane-wave methods	15
5	Computational details	17
5.1	Structure relaxation	17
5.2	Ground-state calculations	20
6	Ground-state configurations	23
6.1	Ground-state search	23
6.2	Results of ground-state searches for all clathrates	30
7	Clathrate properties	36
7.1	Electronic properties	36
7.2	Structural properties	39
7.2.1	Lattice constants	39
7.2.2	Bond distances	40
7.2.3	Occupancy factor	43
8	Conclusions and outlook	49
A	Appendix	55
A.1	Additional convergence tests	55
A.2	Cluster expansion with the PBEsol functional	56

B Appendix	57
B.1 Configurations of Zintl composition (LDA)	57
B.2 First results using the Wang-Landau method	57
B.3 Compressive sensing	59
Abbreviations	60

1 Introduction

Energy generation in an environmentally friendly manner is a key issue of our society. The enormous amount of more than two-thirds of utilized energy is lost as waste heat [1]. The waste heat is produced by engines, refrigerators, air conditioners, computers, *etc.* Its reutilization is highly desired, since often the heat has even to be removed by additional cooling processes.

Thermoelectrics provide a possibility to transform heat into electricity. Thermoelectric devices consisting of many thermoelectric couples are ideal in terms of scalability and reliability since these devices contain no moving parts. Thermoelectric couples are built from an *n*-type (free electrons) and a *p*-type (free holes) material connecting a heat source and a heat sink [1, 2, 3, 4]. A single thermoelectric couple is shown in Fig. 1.1 (left, taken from [5]). The temperature gradient induces a carrier diffusion from regions of high temperature (red) to regions of low temperature (blue) in order to lower the energy of the charge carriers. In case of the *p*-type material (violet), the moving holes produce a current from the hot to the cold end of the material, whereas for the *n*-type material (green), the electrons generate a current from the cold to the hot end. The voltage (V) between the two materials at the heat sink is proportional to the Seebeck coefficient (S): $\Delta V = S\Delta T$. The phenomenon of the Seebeck effect is named after its discoverer Thomas Seebeck [6] and can also be used in the opposite way for thermoelectric cooling (Peltier effect [7]).

The efficiency of a thermoelectric material is determined by its figure of merit

$$zT = \frac{S^2\sigma}{\kappa}T, \quad (1.1)$$

which depends not only on S , but also on the electrical conductivity σ , the thermal conductivity κ , and the temperature T . Trends of their dependencies with respect to the charge-carrier concentration for the example of Bi_2Te_3 are illustrated in Fig. 1.1 (right, taken from [8]). While S decreases, σ increases exponentially with the number of charge carriers. Also, there is an increase of the thermal conductivity. The thermal conductivity consists of two contributions: (i) the electronic part, κ_e , originated by electrons and holes transporting heat and (ii) the lattice part, κ_l , resulting from phonons traveling through the lattice. Usually, κ_e is roughly proportional to the electrical conductivity (Wiedemann-Franz law [9]) confirming its similar behavior to σ in Fig. 1.1.

To reach a large zT (Eq. (1.1)), the conflicting properties of a high σ , a high S , and a small κ have to be combined in one material. Materials with optimal electronic properties (high S and high σ) are crystalline semiconductors. In order to have a material with low thermal conductivity, the lattice part κ_l has to be minimized. Minimal thermal conductivity is achieved in phonon glasses [10] where

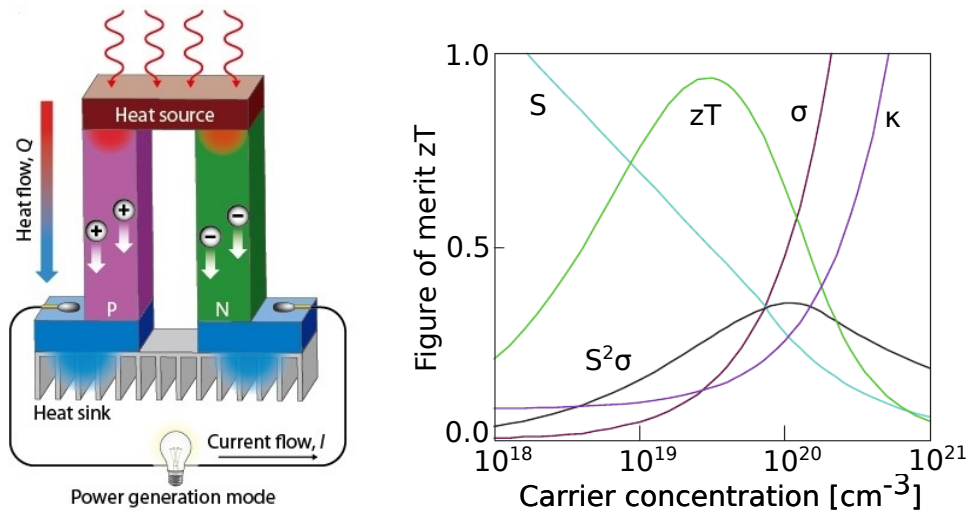


Figure 1.1: Left: Principle of thermoelectric power generation (from Ref. [5]). Right: Optimizing the figure of merit zT with tuning of the carrier concentration (from Ref. [8]).

the energy transport by phonons is regarded as a random walk through the lattice. The combination of high electronic conductivity and low thermal conductivity leads to the concept of the phonon-glass electron-crystal [11] (glass for phonons and crystal for electrons). Materials fulfilling this concept are considered exotic.

Typical thermoelectric materials are the alloys PbTe or SiGe, whose zT reaches 1 (at 500°C) and 0.6 (at 700°C), respectively [3]. Thermoelectrics with $zT \approx 1$ are considered as the first generation. Experimental breakthroughs have been achieved in terms of finding compounds with a low thermal conductivity in the 1990's [3, 12, 13] (second generation). Nowadays, the third generation attains zT values of around 1.8-2.2, as in the case of nanostructures with anisotropic transport properties [3, 13]. Currently, there are many new materials under investigation, as for example skutterudites ($zT \approx 1.7$) [14] and half-Heusler alloys ($zT \approx 1.2$) [15].

In this work, we study the clathrate compounds $\text{Ba}_8\text{Al}_x\text{Si}_{46-x}$ and $\text{Sr}_8\text{Al}_x\text{Si}_{46-x}$ ($6 \leq x \leq 16$), which are promising candidates for high-efficient thermoelectric materials. Chapter 2 introduces the type-I clathrate structure with its large compositional and configurational flexibility. In Chapter 3, the cluster expansion technique and the methodology used to compute the ground-state (GS) configuration of each compound is explained. The *ab-initio* calculations for the clathrate compounds are performed with the density-functional-theory (DFT) package **exciting**. The concepts of DFT and the code **exciting** are briefly described in Chapter 4. The computational details for obtaining the *ab-initio* energies of a clathrate configuration are presented in Chapter 5. The next two chapters cover the results. Chapter 6 addresses the search for the GS configurations of clathrate compounds. Here, the procedure of the GS search for $\text{Ba}_8\text{Al}_x\text{Si}_{46-x}$ is explained in detail, and the results for both compounds are discussed. In Chapter 7, the electronic and structural properties for the GS configurations as well as finite-temperature simulations for the site occupations are presented. Finally, a summary of the findings and an outlook on how to extend the work is given in Chapter 8.

2 Type-I clathrates

This chapter discusses the type-I clathrate compounds. First, their structure with its properties is introduced (Sec. 2.1). Furthermore, a closer look is taken at the compounds $\text{Ba}_8\text{Al}_x\text{Si}_{46-x}$ and $\text{Sr}_8\text{Al}_x\text{Si}_{46-x}$ (Sec. 2.2), which are the subject of this work. At the end, the combinatorial explosion of the configurational space of these materials is demonstrated in Sec. 2.3.

2.1 Clathrate structure

The unit cell of the type-I clathrate structure, shown in Fig. 2.1(a), consists of a cage structure hosting guest atoms (comprising 54 atoms in total). Its crystallographic space group is $Pm\bar{3}n$ (No. 223). The host structure (also called framework) is built from 46 atoms forming eight cages, six tetrakaidehedra and two dodecahedra (Fig. 2.1 (b)). They exhibit three symmetrically distinct sites, the Wyckoff sites $24k$ (indicated by the green color), $16i$ (blue), and $6c$ (red). The eight guest atoms are placed inside the cages at the Wyckoff positions $6d$ and $2a$, respectively (yellow).

The Wyckoff sites of the framework form unique connections to the other sites,

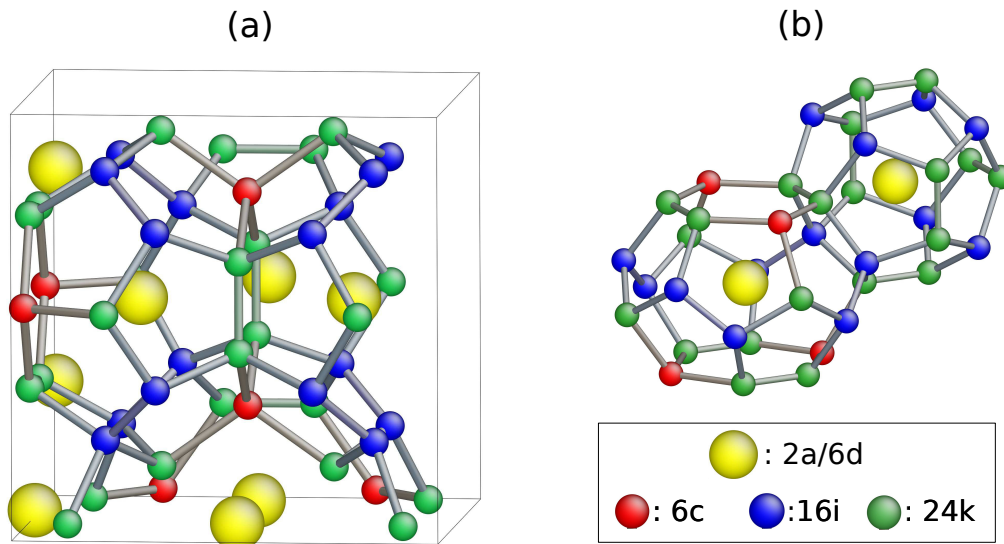


Figure 2.1: Type-I clathrate structure: (a) Unit cell and (b) building block, consisting of large tetrakaidehedral (24-atom) cages and dedecahedral (20-atom) cages. The Wyckoff positions are indicated by different colors: Host atoms at $24k$ in green, at $16i$ in blue and at $6c$ in red. Guest atoms at $2a$ and $6d$ in yellow.

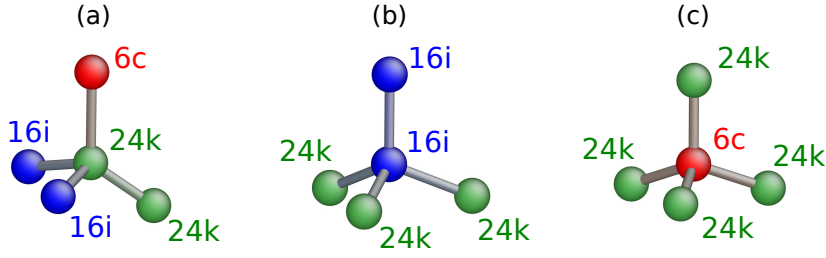


Figure 2.2: Wyckoff sites (a) $24k$, (b) $16i$ and (c) $6c$ of the framework with their neighbor sites.

as shown in Fig. 2.2. Each atom forming tetrahedral covalent bonds is connected to four other sites. The $24k$ (short k) site is connected to another k site, two $16i$ (short i) sites and a $6c$ (short c) site (Fig. 2.2 (a)). The i site is connected to three k sites and another i site (no connection to the c site) (Fig. 2.2 (b)). The c site is only connected to three k sites. In total, the connections result in four different kind of bonds: $k-k$, $k-i$, $k-c$, and $i-i$.

The type-I clathrate compositions are represented by $A_8M_xX_{46-x}$, where M_xX_{46-x} form the host structure and A are the guest atoms. The atoms X are group IV elements of the periodic table (*e.g.*, Si, Ge and Sn). Their 4 valence electrons build the covalent tetrahedral bonds of the framework. Thus, in the absence of guest atoms, the host structure is a semiconductor. The guest atoms A are group II elements (*e.g.*, Sr, Ba, Eu). When inserted into the cages, their 2 valence electrons are donated to the crystal framework. With 8 guest atoms, the crystal framework has 16 additional free electrons (n -doping), therefore, for $x = 0$, a metallic state is expected. These free charges can be compensated by p -doping of the host structure. The p -doping is realized by substituting group-IV elements of the host structure with a group-III element M (*e.g.*, Al, Ga, In). The index x in $A_8M_xX_{46-x}$ indicates the number of substituents. A charge compensated clathrate is expected at $x = 16$ substituents (Zintl composition) [16, 17, 18]. The full charge compensation is based on the assumption that the host-guest interactions are purely ionic and the free charges are completely absorbed by the dopants. Thus, the Zintl composition leads to a semiconductor state, which is highly desired for thermoelectric applications.

The clathrate compounds are promising candidates for exploiting the idea of the phonon-glass electron-crystal. The crystal framework ensures a high performance of the electronic properties (expected to be optimal at the Zintl composition). The guest atoms in the cages induce static and dynamic disorder thereby lowering the thermal conductivity. They are also called “rattlers”, as they are expected to vibrate at low frequencies in a non-directional fashion, efficiently scattering low energy phonons responsible for heat transport. The variety of chemical compositions available for building the clathrate structure offers a playground for optimizing the electronic properties and reaching a high zT . With the substitution of host atoms the charge-carrier concentration can be tuned to its optimum value.

2.2 $Ba_8Al_xSi_{46-x}$ and $Sr_8Al_xSi_{46-x}$

Materials based on Si and Ge are used in the electronic industry for many purposes. The clathrates based on Ge and Ga with their thermoelectric properties are al-

ready well known [19, 20, 21]. For the compound $\text{Ba}_8\text{Ga}_{16}\text{Ge}_{30}$, high thermoelectric properties with possible maximum $zT \approx 1.63$ are reported at $T = 1100$ K [20]. Experimentally, these compounds achieved a $zT \approx 1.35$ with an electrical conductivity $\sigma \approx 600$ $(\Omega\text{cm})^{-1}$ at $T = 1066$ K a Seebeck-coefficient $S \approx -300$ $\mu\text{V}/\text{K}$ at $T = 900$ K, and a thermal conductivity $\kappa \approx (1.24 - 2.10)$ W/mK at $T = 900 - 1200$ K. The Sr-filled clathrate (short Sr clathrate) reveals glass-like thermal conductivity [22, 23] (around 0.008 W/mK for $\text{Sr}_8\text{Ga}_{16}\text{Ge}_{30}$ [22]).

In this work, we focus on the clathrate compounds $\text{Ba}_8\text{Al}_x\text{Si}_{46-x}$ and $\text{Sr}_8\text{Al}_x\text{Si}_{46-x}$. Since the guest atoms, Ba and Sr, have already demonstrated good performance in terms of electronic and thermal properties in Ge-Ga based clathrates, their investigation in another framework is promising. The Al-Si based clathrates are of technological interest in terms of price, weight, and low environmental impact. So far, Al-substituted clathrates could be synthesized in the range $x \leq 15$ for $\text{Ba}_8\text{Al}_x\text{Si}_{46-x}$ [24, 25]. In case of $\text{Sr}_8\text{Al}_x\text{Si}_{46-x}$, only the compound with $x = 10$ could be realized [24]. However, the Zintl composition has not been achieved so far, and the reasons for this are not clear.

2.3 Combinatorial explosion

The configurational space of the clathrate compounds is huge. This becomes clear with an estimate of the number of configurations for a fixed number of substituents. The host structure of the clathrate consists of 46 sites ($N_{\text{sites}} = 46$). The non-substituted clathrates contain only Si atoms at those sites. The maximum number of possibilities to arrange the Al atoms inside the host structures (upper bound) is given by the binomial coefficient $\binom{46}{x}$, with x indicating the number of Si atoms substituted by Al atoms. Some structures are symmetrically equivalent, what reduces the number of distinct structures. A lower bound of the total number of configurations is obtained under the assumption that every structure is symmetrically equivalent to N_{sym} others, where N_{sym} is the total number of symmetry operations, which is 48 for the pristine clathrate. Hence, the number of symmetrically distinct

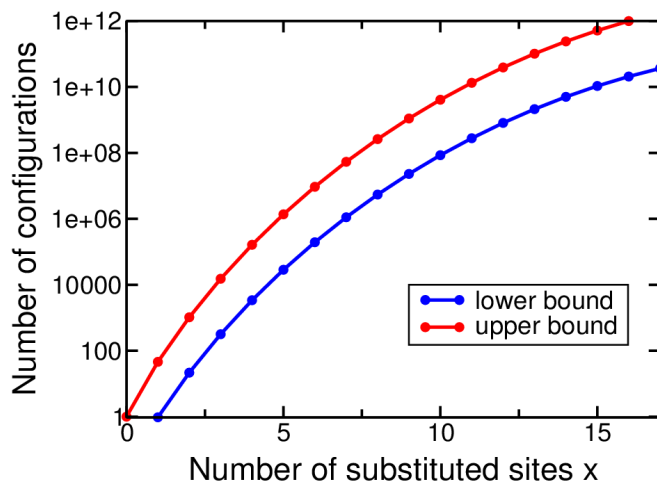


Figure 2.3: Combinatorial explosion of the number of configurations for the clathrate structure.

structures $N_s(x)$ for a certain composition x lies in the following range

$$\frac{1}{N_{\text{sym}}} \frac{N_{\text{sites}}!}{x!(N_{\text{sites}} - x)!} \leq N_s(x) \leq \frac{N_{\text{sites}}!}{x!(N_{\text{sites}} - x)!}, \quad (2.1)$$

and the lower and upper bound differ by the factor $1/N_{\text{sym}}$.

Figure 2.3 shows the upper and lower bound from Eq. (2.1) for x between 1 and 16. The number of structures increases with the number of substituents almost exponentially. For $x=16$, there are $N_s > 2 \times 10^{10}$ structures, and the maximum is reached at half occupancy ($x = 23$).

The large configurational space of clathrates demands a special procedure to obtain the ground-state configurations in an efficient way, due to the impossibility of performing *ab-initio* calculations for all candidate materials. A powerful tool for this purpose is the cluster expansion technique, which will be explained in the next chapter.

3 Cluster-expansion approach

The cluster expansion (CE) enables to predict a property of interest for an arbitrary configuration by performing *ab-initio* calculations for only a small set of structures. The underlying assumption of the CE technique is the configurational dependence of the compound's properties, such as the energy, the band gap, lattice constant, *etc.*

This chapter is organized as follows: Section 3.1 introduces the formalism of the CE. Afterwards, criteria to determine the predictability power of the CE technique are described in Sec. 3.2. In Sec. 3.3, two commonly used implementations of CE are discussed, and the new CE code, called **CELL**, used to explore the clathrate compounds, is introduced.

3.1 Formalism

In this section, the theoretical background of the CE is presented. The formalism is a generalization of the well-known Ising model, where spins are placed at the sites of a rigid lattice, and the two possible states at one site are spin up or spin down. In case of a substitutional problem, *e.g.*, a binary alloy, the lattice sites are occupied with two different atom species, either type A or type B, representing the two occupation states. The CE approach can be extended to multicomponent systems, generally introduced in Ref. [26].

In practice, a supercell is built from a set of periodic repetitions of the so-called parent cell. An occupation variable σ_i is assigned to each site i of the supercell. It can take the value either -1 or $+1$. For clathrates, the site types are the species Al ($\sigma = +1$) or Si ($\sigma = -1$). Suppose the supercell consists of N sites, the structure s is described by a particular occupation of these sites, the occupation vector

$$\boldsymbol{\sigma}_s = (\sigma_{s1}, \sigma_{s2}, \dots, \sigma_{sN}) . \quad (3.1)$$

A set of sites defines a cluster α . The cluster can consist of zero sites (the empty cluster), one site (1-point cluster), two sites (2-point cluster), or even more sites (N_{points} -point cluster), where N_{points} specifies the number of points building the cluster. The correlation between the structure s and the cluster α is defined as

$$X_{s\alpha} = \frac{1}{m_\alpha} \sum_{\beta \equiv \alpha} \prod_{i \in \beta} \sigma_{si} = \langle \prod_{i \in \beta} \sigma_{si} \rangle , \quad (3.2)$$

where β are all clusters which are equivalent to α with respect to symmetry operations from \mathcal{R} . Here, \mathcal{R} is the set of symmetry operations of the space group of the parent lattice. The multiplicities m_α represent the number of clusters symmetrically

equivalent to α . Thus, the correlation is an average over symmetrically equivalent clusters and can take any real value in the range $[-1, +1]$.

With an appropriate selection of N_α symmetrically distinct clusters, the property P of a given structure s can be parametrized by a polynomial of the correlation matrix $X_{s\alpha}$ as follows:

$$\hat{P}_s = \sum_{i=1}^{N_\alpha} m_{\alpha_i} J_{\alpha_i} X_{s\alpha_i} \quad (3.3)$$

The coefficients J_α are called effective cluster interactions (ECI). The ECIs are calculated by fitting them to a set of structures N_s from which the quantities P are known by first principles calculations. A detailed explanation follows in the next section.

Equation (3.3) can be recast in a matrix-vector representation as follows:

$$\begin{pmatrix} \hat{P}_1 \\ \hat{P}_2 \\ \vdots \\ \hat{P}_{N_s} \end{pmatrix} = \begin{pmatrix} X_{1\alpha_1} & X_{1\alpha_2} & \cdots & X_{1\alpha_{N_\alpha}} \\ X_{2\alpha_1} & X_{2\alpha_2} & \cdots & X_{2\alpha_{N_\alpha}} \\ \vdots & \vdots & \ddots & \vdots \\ X_{N_s\alpha_1} & X_{N_s\alpha_2} & \cdots & X_{N_s\alpha_{N_\alpha}} \end{pmatrix} \cdot \begin{pmatrix} m_{\alpha_1} J_{\alpha_1} \\ m_{\alpha_2} J_{\alpha_2} \\ \vdots \\ m_{\alpha_{N_\alpha}} J_{\alpha_{N_\alpha}} \end{pmatrix} \rightarrow \hat{P} = X\tilde{J}. \quad (3.4)$$

Here, $\tilde{J}_\alpha = m_\alpha J_\alpha$.

The CE predicts the property P by taking advantage of the unique configurational dependence of the system of interest. If a CE is built using the set of clusters given by all possible symmetrically distinct configurations of the supercell, then a perfect fit to the property can be obtained. In practice, the CE method has proven rapid convergence with respect to the number of clusters necessary to catch the physics of the system. For alloys, around 15 to 20 ECIs of short-range pairs, triples, and quadruplets and the usage of about 40-60 first principles calculations lead to a converged CE [27, 28].

3.2 Search for a CE with high validity

The optimal ECIs of the CE are calculated with a least-squares fit, which minimizes the mean-squared error (MSE)

$$\text{MSE}^2 = \frac{1}{N_s} \sum_{i=1}^{N_s} (P_i - \hat{P}_i)^2. \quad (3.5)$$

The property P_i of structure i is known from *ab-initio* calculations, and \hat{P}_i is the value predicted by the CE. The MSE is an ℓ_2 norm. The general definition of the ℓ_p norms is given by

$$\|u\|_p = \left(\sum_i |u_i|^p \right)^{1/p}, \quad (3.6)$$

where the ℓ_1 norm (Manhattan distance) and the ℓ_2 norm (Euclidean distance) are special cases.

However, the MSE does not capture the transferability of the model to new structures. To evaluate the prediction error of the CE, the cross-validation (CV),

$$\text{CV}^2 = \frac{1}{N_s} \sum_{i=1}^{N_s} (P_i - \hat{P}_{(i)})^2, \quad (3.7)$$

is a suitable measure [29, 30]. Here, $\hat{P}_{(i)}$ is the predicted value of P_i obtained from the least-squares fit of $(N_s - 1)$ data points excluding the data of P_i .

The CV obtained from the exclusion of one data point at a time, as in Eq. (3.7), is called the leave-one-out CV (LOO-CV) and is widely used [28, 29, 30, 31]. In Ref. [32], the leave-many-out CV (LMO-CV) is suggested as an alternative way. Here, the data set is split into a *validation data set* with size d and a *construction data set* with the size $(N_s - d)$. The fit is executed with the construction data set and the prediction error is estimated with the validation set. This procedure is repeated for different construction and validation sets to obtain an average. Which definition of the CV provides the best method to estimate the predictive power, typically depends on the system. Therefore, we keep track of both methods but with the focus on the LOO-CV.

An analytic expression to calculate the optimal set of interactions, which minimizes the MSE, can be derived by inserting Eq. (3.4) in Eq. (3.5) and solving for $\partial(\text{MSE}^2)/\partial\tilde{J}_\alpha = 0$. One obtains the optimal ECIs with

$$\tilde{J} = (X^T X)^{-1} X^T P. \quad (3.8)$$

In general, the least-squares fitting method requires a data set that is larger than the number of unknown coefficients. Additionally, this method can lead to an overfitting since the model is trained to reproduce the fitting data. The overfitting may imply fitting to noise in the training data, which spoils the predictive power of the model.

There are several ways of dealing with the problem of overfitting. Typically, they consist in adding “penalization” terms to Eq. (3.5). Once a set of interactions is considered as physically meaningful, only small changes of them are desired if additional clusters are included in the CE. The optimal interactions \tilde{J} with the restriction of allowing only small changes of a subset of physically relevant ECIs, \tilde{J}_α^0 , (usually obtained from a previous optimization with a smaller cluster set), can be achieved by the minimization of

$$S^2 = \frac{1}{N} \sum_{i=1}^N (P_i - \hat{P}_i)^2 + \sum_{\alpha \in \{\gamma\}} A_\alpha (\tilde{J}_\alpha - \tilde{J}_\alpha^0)^2. \quad (3.9)$$

The penalization term represents the second ℓ_2 norm in this equation, and its strength can be tuned through the “penalization vector” \mathbf{A} . Typically, we set A_α to a common value A for the set of physically relevant clusters and to zero for the rest. The analytic result for the optimal ECIs with this penalization term is obtained by solving for $\partial S^2/\partial\tilde{J}_\alpha = 0$, with the result

$$\tilde{J} = (NA + X^T X)^{-1} X^T P + (NA + X^T X)^{-1} NA \tilde{J}^0. \quad (3.10)$$

Due to the additional term NA in the inverted matrix, fitting to a set of clusters larger than the set of *ab-initio* data is possible. Otherwise the rank of the matrix $X^T X$ is lower than its dimension and it cannot be inverted.

An efficient alternative to the minimization of the MSE is provided by the compressive sensing (CS) technique. The CS extracts the interactions of relevant clusters from a pool of clusters without any presumptions, whereas the non-relevant interactions are set to zero. The key interactions are found by using only a data set whose size is proportional to the number of non-zero interactions [33]. The optimal ECIs of CS are given by

$$\min_{\tilde{J}} \left[\frac{1}{2} (\|P - X\tilde{J}\|_2)^2 + \mu \|\tilde{J}\|_1 \right], \quad (3.11)$$

where μ determines the sparseness of the solution, but keeps control of the accuracy at the same time. High values of μ result in a sparse solution with large fitting errors, while small values of μ give dense solutions with a smaller predictive power. For Eq. (3.11), there exists no analytic solution, and it has to be solved by an iterative numerical approach. Such approach is provided by the least absolute shrinkage and selection operator (LASSO) method [34, 35].

For the ground-state search of the clathrate compounds, we evaluate the predictive power of the CE with the LOO-CV and LMO-CV. They are performed with the least-squares fit with and without the penalization term since there exists an analytic solution for the optimal ECIs. The CS method is left for cross-checking.

3.3 Realization of the cluster expansion

There exist different codes to construct a CE making this method applicable to a variety of purposes. This section explains why the available software packages reach their limits regarding large parent cells, as is the case with the unit cell of the clathrate compounds with $N_{\text{sites}} = 46$ (Sec. 3.3.1). Furthermore, an alternative implementation is introduced, the python package **CELL**. **CELL** provides a solution for the CE with large parent cells (Sec. 3.3.2). In the context of this work, the property P to be predicted by the CE is always the energy E since the CE is used to determine the GS configuration. In general, it can be replaced by any other property of the system which depends on the structural configuration.

3.3.1 Common cluster expansion codes

Two computational tools commonly used to perform a CE are the **Alloy Theoretic Automated Toolkit**, ATAT [30] (open source), and the **UNiversal CLuster Expansion**, UNCLE [36].

ATAT and UNCLE have similar working procedures which are sketched in a joint workflow in Fig. 3.1 (a). Structure selection phases (green) are followed by *ab-initio* calculations which are used to construct a CE (yellow). At the beginning, each code starts with a full structure enumeration for all compositions (green box in red frame) to achieve the complete set of symmetrically-distinct configurations. An initial set of structures from the complete set of configurations is selected, their *ab-initio* values of the energy E are calculated, and the CE is executed. For the CE, a cluster optimization is performed by selecting different sets of clusters and choosing the set that yields the smallest CV. In ATAT, a set of clusters is specified by the maximum site distance and the maximum number of points N_{points} of the clusters, up to which clusters are considered, whereas UNCLE uses a genetic algorithm [37, 38] for the cluster selection. In a next step, new structures from the set of configurations are selected to improve the CE. The calculated *ab-initio* energies of this new set of structures are added to construct a new CE. The structure selection phase followed by the calculation of their *ab-initio* energies and an improved CE, represents a single iteration. The optimal set of clusters can change for each iteration. The loop is repeated until the CV is low enough.

Besides the *ab-initio* calculations, the structure selection phases of the workflow in Fig. 3.1 (a) involves two computationally intensive parts with regard to time and memory:

- The full enumeration of symmetrically distinct structures;
- The prediction of the property E for the complete configurational space.

These parts constitute an almost impossible task for clathrates with their large configurational space. The inefficiency of these two tasks are explained in detail in the following paragraphs:

The structure enumeration consists of two parts: (i) finding all symmetrically distinct supercells for a given number of sites, and (ii) finding all symmetrically distinct configurations in each supercell. Concerning the second part, ATAT and UNCLE scan the structures one by one and check their symmetrical equivalence to the previously examined structures. For (i), UNCLE uses an efficient strategy [39] with linear scaling on the number of sites. However, part (ii) is still very demanding and would take several weeks for even a small range of clathrate compositions. For a cell with $N_{\text{sites}} = 32$ and thus, $2^{32} \approx 10^{10}$ configurations, which have to be examined in order to obtain the symmetrically distinct configurations, the CPU time is reported to be one week [39].

The second computationally intensive step in the workflow is the calculation of the predicted energy \hat{E} for the complete configurational space. This step is needed to determine the GS and to select new structures for improving the CE. In order to get a feeling of the computational cost, we count each operation in Eq. (3.4) and multiply by the time of a single floating point operation (FLOP). The result for N_s structures is

$$T = T_{\text{FLOP}} N_s N_\alpha (2 + N_m N_{\text{points}}). \quad (3.12)$$

The number of structures N_s is given by Eq. (2.1). We compute minimal and maximal times (T_{min} and T_{max}) from the lower and upper bounds for N_s (obtained from Eq. (2.3)). The value N_m defines the average of the multiplicities of all N_α clusters considered in the CE. In the case of the clathrates, a typical set of clusters consists of clusters up to triplets ($N_{\text{points}} = 3$) and up to a radius 4 \AA , which corresponds to $N_\alpha = 34$ and $N_m = 33$ (T_{FLOP} time is estimated to be $T_{\text{FLOP}} = 10^{-7} \text{ s}$). The estimated CPU time for the composition range $x \in [6, 16]$ is shown in Tab. (3.1). For

x	T_{min}	T_{max}
6	1.5 min	1 h
7	8.5 min	7 h
8	40 min	1.5 days
9	3 hours	6 days
10	11 hours	3 weeks
11	1.5 days	2.5 months
12	30 days	7 months
13	1.6 weeks	1.5 years
14	4 weeks	4 years
15	2 months	8 years
16	4 months	15 years

Table 3.1: Estimated computing time to predict \hat{E} of all symmetrically-distinct structures Eq. (3.12). All 3-point clusters ($N_{\text{points}} = 3$) up to a radius of 4 \AA for the clathrate compound are considered.

$x = 16$, the minimal time reaches already 4 months, whereas it takes over incredible 15 years for $x = 16$ in the worst case.

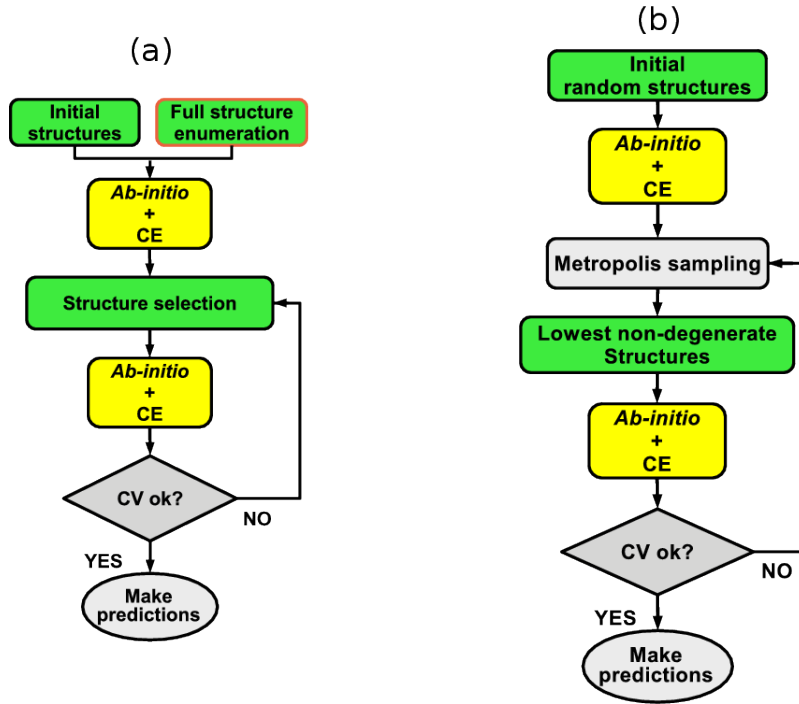


Figure 3.1: Workflow of ATAT and UNCLE (left) and CELL (right) to perform a CE: It consists of structure selection phases (green) followed by *ab-initio* calculations with the CE construction (yellow). (a) ATAT and UNCLE with a full enumeration at the beginning, (b) CELL with an importance sampling of the configurational space based on the Metropolis algorithm.

3.3.2 CELL - cluster expansion with large parent cells

To avoid a full enumeration of the symmetrically distinct set of structures and a full calculation of the predictions of E , the large configurational space of clathrates has to be explored in an efficient way to determine the GS. A solution is provided by the code **Cluster Expansion with large parent cellLLs**, short **CELL**. **CELL** has been developed in our research group [40]. I contributed several modules to the code, which are used for this thesis. These are compressed sensing with LASSO, the LMO-CV, the generation of the ECIs with ℓ_2 penalization, and the Wang-Landau method (see Appendix, Sec. B.2).

The workflow is shown in Fig. 3.1(b). It adopts the iterative methodology consisting of structure selection phases (green) and the calculation of the *ab-initio* energies followed by the CE (yellow). However, the full enumeration of the configuration space is avoided and the working procedure starts with a selection of randomly generated structures. Their *ab-initio* energies are calculated, and a CE is performed. Instead of predicting the energies of each possible configuration with the CE, an efficient importance sampling (light gray) of the configurational space is performed for each composition. This sampling is done with the Metropolis-Hasting algorithm, that is used to propose a new lowest non-degenerate structure for each composition. In the next iteration, the *ab-initio* energies from the new set of lowest non-generate

structures lead to an improvement of the CE. This procedure is repeated until the CV is small enough to make predictions.

Taking a closer look at the sampling, the Metropolis sampling (MS) explores the configurational space in the following way:

1. Start with a random configuration σ_1 .
2. Predict the energy \hat{E}_1 of σ_1 with the CE and set $E_{\min} = \hat{E}_1$.
3. Set $N_{\text{sampl}} = 0$.
4. Generate a new configuration σ_2 by swapping two atoms (swapping occupation variables of two sites) and predict its energy \hat{E}_2 .
5. Accept the new configuration σ_2 with the probability $\min(1, \exp(-\Delta\hat{E}/kT))$ with $\Delta\hat{E} = \hat{E}_2 - \hat{E}_1$:
 - For $\Delta\hat{E} \leq 0$, the new configuration is energetically preferred and is accepted with the probability 1.
 - For $\Delta\hat{E} \geq 0$, the new configuration is energetically NOT preferred and is taken with the probability $\exp(-\Delta\hat{E}/kT)$. k is the Boltzmann constant and T the temperature, which should be appropriately chosen.
6. If $\hat{E}_2 < E_{\min}$, set $E_{\min} = \hat{E}_2$ and go back to point 3.
7.
 - If $N_{\text{sampl}} < N_{\text{sampl}}^{\text{MAX}}$, set $N_{\text{sampl}} = N_{\text{sampl}} + 1$ and go back to point 4.
 - If $N_{\text{sampl}} = N_{\text{sampl}}^{\text{MAX}}$, a new lowest non-degenerate structure with E_{\min} is found.

The energies of the structures for which the *ab-initio* energies have already been calculated are also predicted with the CE, but are excluded from the MS. If the MS finds a new lowest non-degenerate structure whose predicted energy is higher than the energy of GS, a new GS could not be obtained. This fact could indicate that the GS was already found with a previous CE. In order to make sure that the sampling reaches the GS, one has to explore different numbers of sampling steps $N_{\text{sampl}}^{\text{MAX}}$. Also, it is important to sample at different temperatures. At low temperatures, the MS may explore only a small region of possible configurations due to a barrier in the energy landscape which separates two regions of configurations. High temperatures, conversely, avoid a trapping at local minima of the energy landscape, but make less probable to sample GS configurations.

In general, we need to keep in mind that the GS prediction is also limited by the accuracy of the *ab-initio* data. Small changes of the structures cannot be distinguished by the CE if the *ab-initio* energies also do not capture the related energy differences in an accurate way.

4 *Ab-initio* calculations with DFT

The *ab-initio* energies are obtained using density-functional theory (DFT). They are calculated with the full-potential all-electron DFT package **exciting** [41]. In Sec. 4.1, the Kohn-Sham equations and the exchange-correlation energy functionals used for the *ab-initio* calculations are explained. Section 4.2 briefly introduces the linearized augmented plane-wave method as implemented in **exciting**.

4.1 Kohn-Sham equations

Solving the many-body Schrödinger equation is a very demanding task, and approximations are unavoidable. Within DFT, Kohn and Sham [42] demonstrated a way to map a system of interacting particles onto a fictitious system of non-interacting particles, with the same electronic density as the interacting one. Thus, the problem of solving the Schrödinger equation of N interacting particles ($3N$ degrees of freedom) is reduced to the problem of a single-particle Schrödinger equation (with only 3 degrees of freedom). This single-particle Schrödinger equation of the fictitious system is called Kohn-Sham equation:

$$\left[-\frac{1}{2}\nabla^2 + v_{\text{KS}}(\mathbf{r}) \right] \psi_i(\mathbf{r}) = \epsilon_i \psi_i(\mathbf{r}) . \quad (4.1)$$

Here, $\psi_i(\mathbf{r})$, ϵ_i , and $v_{\text{KS}}(\mathbf{r})$ are the wavefunctions, the eigenenergies, and the potential of the KS system, respectively. The electronic density of this system is obtained from the single-particle Kohn-Sham wavefunctions by

$$n(\mathbf{r}) = \sum_{i=1}^N |\psi_i(\mathbf{r})|^2 . \quad (4.2)$$

Furthermore, the Kohn-Sham potential, given by

$$v_{\text{KS}}(\mathbf{r}) = v_{\text{ext}}(\mathbf{r}) + v_{\text{H}}(\mathbf{r}) + v_{\text{xc}}(\mathbf{r}) , \quad (4.3)$$

is the sum of the external potential $v_{\text{ext}}(\mathbf{r})$ generated by the ions, the Hartree potential $v_{\text{H}}(\mathbf{r})$ representing the classical Coulomb interaction, and the exchange-correlation potential $v_{\text{xc}}(\mathbf{r})$. $v_{\text{xc}}(\mathbf{r})$ is defined as the functional derivative of the exchange-correlation energy E_{xc} with respect to the density:

$$v_{\text{xc}}(\mathbf{r}) = \frac{\delta E_{\text{xc}}[n]}{\delta n(\mathbf{r})} . \quad (4.4)$$

As $v_{\text{KS}}(\mathbf{r})$ depends on the density, the Kohn-Sham equations have to be solved self-consistently. First, with an initial guess for $v_{\text{KS}}(\mathbf{r})$, the Kohn-Sham equations are

solved and from the obtained $\psi_i(\mathbf{r})$'s the density $n(\mathbf{r})$ is calculated. With the new $n(\mathbf{r})$, $v_{\text{KS}}(\mathbf{r})$ is calculated and the Kohn-Sham equations are solved again to obtain an improved $n(\mathbf{r})$. This procedure is repeated until $v_{\text{KS}}(\mathbf{r})$ and $n(\mathbf{r})$ are converged. The number of repetitions defines the number of self-consistency field (SCF) steps (also called SCF iterations).

In principle, the KS scheme is exact for the GS if the exact $v_{\text{xc}}(\mathbf{r})$ is known. However, $E_{\text{xc}}[n]$ and $v_{\text{xc}}(\mathbf{r})$ are not known, thus they have to be approximated. Several approximations have been developed during the years, with different levels of complexity. The simplest approximation is the local-density approximation (LDA). In the LDA, the exchange-correlation energy is given by

$$E_{\text{xc}}^{\text{LDA}} = \int e_{\text{xc}}^{\text{hom}}(n(\mathbf{r})) n(\mathbf{r}) d\mathbf{r}, \quad (4.5)$$

where $e_{\text{xc}}^{\text{hom}}(n)$ is the exchange-correlation energy of a homogeneous electron gas of density n (independent of \mathbf{r}). The exchange part of $e_{\text{xc}}^{\text{hom}}(n)$ is analytically known and the correlation part can be estimated with high accuracy ($\pm 1\%$ using Monte Carlo methods [43, 44]). In this thesis, the LDA functional parametrized by Perdew and Wang [45] is used for the *ab-initio* calculations with LDA. Furthermore, the generalized gradient approximation (GGA) is used where the exchange-correlation energy depends not only on $n(\mathbf{r})$ but also on its gradient $\nabla n(\mathbf{r})$. In this work, we use PBEsol, a GGA functional optimized for solids [46].

4.2 Linearized augmented plane-wave methods

The package `exciting` [41] implements several variants of the linearized augmented plane-wave method for solving the Kohn-Sham equations (see Ref. [41] and references therein). The KS wavefunctions are represented by a superposition of augmented plane-waves $\phi_{\mathbf{G}+\mathbf{k}}(\mathbf{r})$:

$$\psi_{i\mathbf{k}}(\mathbf{r}) = \sum_{\mathbf{G}}^{|\mathbf{G}| < G_{\text{max}}} C_{i\mathbf{G}}^{\mathbf{k}} \phi_{\mathbf{G}+\mathbf{k}}(\mathbf{r}). \quad (4.6)$$

Here, \mathbf{k} are the wave vectors in the first Brillouin zone and \mathbf{G} are the reciprocal lattice vectors. The space is separated into muffin-tin (MT) regions defined as spheres with radius R_{MT}^{α} around the nuclei located at \mathbf{R}_{α} and the interstitial (I) region, defined as the region between the MTs. Accordingly, a dual representation of the basis functions is used and defined as follows:

$$\phi_{\mathbf{G}+\mathbf{k}}(\mathbf{r}) = \begin{cases} \sum_{lm} A_{lm\alpha}^{\mathbf{G}+\mathbf{k}} u_{l\alpha}(r_{\alpha}) Y_{lm}(\hat{\mathbf{r}}_{\alpha}), & r_{\alpha} = |\mathbf{r} - \mathbf{R}_{\alpha}| \leq R_{\text{MT}}^{\alpha} \\ \frac{1}{\sqrt{\Omega}} e^{i(\mathbf{G}+\mathbf{k})\cdot\mathbf{r}}, & \mathbf{r} \in I. \end{cases} \quad (4.7)$$

In the MT region, the Kohn-Sham wavefunctions are expanded in terms of spherical harmonics $Y_{lm}(\hat{\mathbf{r}}_{\alpha})$ and radial functions $u_{l\alpha}(r_{\alpha})$, whereas the interstitial region is represented by plane-waves. The coefficients $A_{lm\alpha}^{\mathbf{G}+\mathbf{k}}$ are used to match the plane-waves with the functions of each MT at the MT sphere.

The basis as defined in Eq. (4.7) leads to a non-linear eigenvalue problem to find the exact Kohn-Sham wavefunctions $\psi_{i\mathbf{k}}(\mathbf{r})$, because the radial part $u_{l\alpha}$ depends on the eigenenergies of the Kohn-Sham system. In order to linearize the eigenvalue equation and make it easily tractable two strategies are available: The linearized

APW (LAPW) method and the APW local-orbital (APW+lo) method. In the first scheme, instead of energy-dependent radial functions, a linear combination of radial functions at fixed energies and their energy derivatives is used. The condition of continuous derivative at the MT is added in order to fix the additional coefficient related to this linear combination. The second scheme consists in keeping the APW from Eq. (4.7), but with frozen energy parameters, and add linearly-independent local orbitals, defined in terms of a linear combination of the radial function and its energy derivatives at fixed energy parameter. These local orbitals are non-zero strictly within MTs, and slightly increase the size of the basis set. The APW+lo method provides more flexibility and yields smaller errors in the eigenvalues than LAPW for the same basis set size [41]. In this work, we have used a combination of these two augmentation types.

The basis set used to describe the system in terms of Hamiltonian matrices with finite size is truncated by the plane-wave cutoff G_{\max} with $G_{\max} > |\mathbf{G} + \mathbf{k}|$. The basis set not only depends on this cutoff, but also on the MT radius R_{MT} . A small R_{MT} leads to space in the interstitial region where the wavefunctions vary more rapidly and a larger G_{\max} is needed to reach the same accuracy as for a large R_{MT} . Thus, an appropriate measure of the accuracy of the *ab-initio* calculation is the product $R_{\text{MT}}G_{\max} = \text{rgkmax}$ (R_{MT} refers to the species with the smallest muffin tin sphere). At a fixed R_{MT} , the increase of **rgkmax** causes an increase of G_{\max} , which, in turn, leads to a larger size of the Hamiltonian matrices. In practice, the dimensionless value **rgkmax** is one of the input parameters in **exciting**. Furthermore, the \mathbf{k} -space of the Brillouin zone is discretized with a \mathbf{k} -grid, which is also essential for the accuracy of the *ab-initio* calculations. Whose choice is defined by the integer triple **k-grid** = (n_1, n_2, n_3) , where n_j is the number of \mathbf{k} -points in the j -dimension in \mathbf{k} -space. The computational details about the convergence procedure to achieve good *ab-initio* energies are explained in the next chapter.

5 Computational details

The construction of the CE is based on a set of *ab-initio* energies. Well converged *ab-initio* calculations are essential to obtain a CE with high predictive power. In order to obtain accurate *ab-initio* energies, first full structure relaxations are required (discussed in Sec. 5.1). It is important that the energy differences for different structures of a fixed composition are well converged with respect to the simulation parameters (Sec. 5.2). From an analysis of the energy differences of the GSs for different configurations, it becomes clear that an accuracy below 1 meV/atom is required. For this reason, an additional highly accurate GS calculation is performed for the final geometry of this relaxation process.

5.1 Structure relaxation

The structure relaxation consists of two parts:

- Cell relaxation: Determination of the optimal lattice constant a which minimizes the energy of the cubic unit cell. Desired accuracy: $\Delta a < 0.01 \text{ \AA}$.
- Atom relaxation: Determination of the optimal atomic positions where the components F of the forces acting upon the atoms are below a threshold of $F_{\text{tol}} = 2.5 \text{ mRy/atom}$.

Since the atomic forces depend on the cell volume, alternating cell and atom relaxations are required. Typically, two cycles are enough to reach convergence.

For the cell relaxation, we devised a special optimization routine based on the simplex method of Nelder and Mead [47]. As input parameters, the initial a , an initial step size of the change in a between different steps, and tolerances for the energy and a are chosen. The simplex method approaches with each step the a with the lowest energy until the proposed changes in a and their associated energies are below the chosen input tolerances. In order to obtain the desired accuracy in a and, at the same time, avoid numerous steps, the cell optimization combines the simplex method with a fit of data points $(a, E(a))$ to the Birch-Murnaghan (BM) equation of state [48]. The energy $E(a)$, obtained from the BM equation,

$$E(a) = E_0 + \frac{9B_0}{16}a_0^3 \left\{ \left[\left(\frac{a_0}{a} \right)^2 - 1 \right]^3 \cdot B'_0 + \left[\left(\frac{a_0}{a} \right)^2 - 1 \right]^2 \cdot \left[6 - 4 \left(\frac{a_0}{a} \right)^2 \right] \right\} \quad (5.1)$$

depends on four fit parameters: the optimal lattice constant a_0 , the minimal energy E_0 , the bulk modulus B_0 , and the derivative of the bulk modulus B'_0 . Thus, at least

four data points ($a, E(a)$) are required for the fit. Here, usually the following strategy is used: First, five steps of the simplex method are performed and afterwards, a fit with Eq. (5.1) yields the new a_0 for the sixth (and last) step. Then, the complete cell-relaxation proceeds with six DFT runs, and the optimal lattice constant is obtained by a final fit of Eq. (5.1) to the six obtained data points.

An important role for the cell relaxation is played by the convergence of the energy *difference* between the DFT runs with different a . Realizing that these differences converge much more rapidly than the absolute total energies, we use them as a convergence criterion for the cell-relaxation routine. The first DFT calculation assumes the role of a “guide” run and has a small energy tolerance $E_{\text{tol}}(\text{guide}) = 0.2 \text{ meV}$ for the SCF loop, requiring a large number of SCF iterations. For the following DFT runs, the convergence criterion is the energy difference with respect to the guide run, which is also set to $\Delta E_{\text{tol}} = 0.2 \text{ meV}$. This energy *difference* requires less SCF iterations. An example is shown in Fig. 5.1. The left panel illustrates the

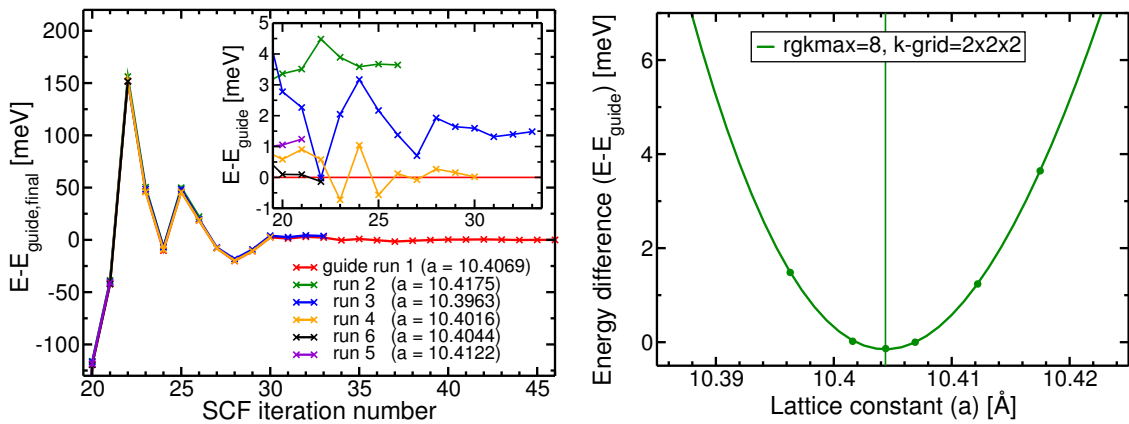


Figure 5.1: Example of the lattice relaxation for a cubic system using the simplex method of Nelder and Mead and a fit with the Birch-Murnaghan equation of state for the Ba clathrate ($x = 10$, LDA). Left: Convergence of the energy differences. Right: Fit of the energy differences vs. the lattice constant a .

total energies, where the zero of the energy corresponds to the converged final value from the guide run ($E_{\text{guide,final}}$). The run for $a = 10.4016 \text{ Å}$ (orange line) stops after 30 iterations, whereas the run for $a = 10.4044 \text{ Å}$ (black line) stops already after 22 iterations. The inset shows the convergence of the energy differences with respect to the guide run (therefore, $E - E_{\text{guide}} = 0$ (x -axis) corresponds to the guide run (red)). In the last iterations of each run, the energy differences are in the range of ΔE_{tol} , whereas the total energy still shows larger fluctuations. Fig. 5.1 (right) shows the fit of Eq. (5.1) to these data points, which match very well. In most cases, the uncertainties are below 10^{-4} meV for E_0 and below 10^{-3} Å for a_0 . Thus, they do not lead to any relevant error for Δa .

The quality of the DFT calculations itself is also relevant for the cell relaxation. The accuracy of the DFT calculation depends mainly on two parameters, **k-grid** and **rgkmax**. **k-grid** controls the level of discretization of the Brillouin zone. **rgkmax** controls the number of augmented plane-waves, *i.e.*, the size of the basis, as described in Sec. 4.2. In Figure 5.2 (left) two cell relaxations for the same **rgkmax**=6 but different **k-grid** are shown for the Ba clathrate as an example. (A similar plot is shown for the Sr clathrate in the appendix, Sec. A.1.) The **k-grid** does not strongly affect the minimum of a , and the distance between the two minima (indicated by

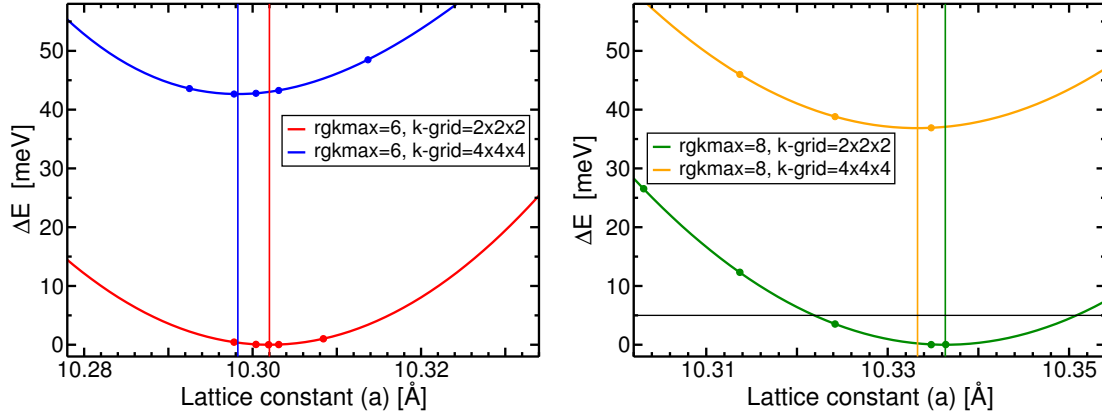


Figure 5.2: Convergence test of the lattice constant for the Sr clathrate ($x = 15$, LDA). Fit of the energy versus the lattice constant a , for $\text{rgkmax}=6$ (left) and $\text{rgkmax}=8$ (right). The minimum of the red (green) curve is chosen as zero in the left (right) panel. Energy difference between the minima is 3.48 eV.

the two vertical lines) is around $\Delta a_0 \approx 0.004 \text{ \AA}$. Analogously, the right panel of Fig. 5.2 shows the same behavior for a larger rgkmax of 8. The change of the \mathbf{k} -grid again only results in a small change of a_0 ($\Delta a_0 = 0.003 \text{ \AA}$). The energy changes associated to this Δa_0 is below the horizontal black line, which indicates the 1 meV/atom threshold for the accuracy. However, the effect of rgkmax on a_0 is much larger: By changing rgkmax from 6 to 8 the equilibrium lattice parameter changes by $\Delta a_0 \approx 0.035 \text{ \AA}$.

In the following, we consider as reference calculation the one performed using \mathbf{k} -grid=4×4×4 and $\text{rgkmax}=8$. For the reference, one obtains the value a_0^{REF} . Using other choices of parameters for the cell relaxation, the optimal lattice constant $a_0(\mathbf{k}\text{-grid}, \text{rgkmax})$ is obtained. In Tab. (5.1), we present the value of

$$\Delta a_0(\mathbf{k}\text{-grid}, \text{rgkmax}) = a_0(\mathbf{k}\text{-grid}, \text{rgkmax}) - a_0^{\text{REF}}. \quad (5.2)$$

The cell relaxation is more sensitive to the value of rgkmax than to \mathbf{k} -grid. The increase of rgkmax from 8 to 9 changes a_0 only by 0.002-0.005 \AA . Thus, for the desired accuracy of the lattice constant below 0.01 \AA , the suitable parameters for a cell relaxation are finally a rgkmax of 8 and a \mathbf{k} -grid of 2×2×2.

Next, we consider the effect of the atom relaxation, defined as the relaxation of the atomic coordinates inside the unit cell for a given lattice constant. The threshold of the forces for atom relaxations is set to $F_{\text{tol}} = 2 \text{ mRy}/a_B$. We define a reference system for which the atom relaxation is performed with \mathbf{k} -grid=4×4×4 and $\text{rgkmax}=8$. The module of the maximum force in this system determines a reference force $F_{\text{relax}}^{\text{REF}}$. Atom relaxations are performed for different rgkmax and \mathbf{k} -grids.

$\Delta a_0 [\text{\AA}]$ for Ba ($x=6$)				$\Delta a_0 [\text{\AA}]$ for Sr ($x=15$)		
rgkmax	6	8	9	rgkmax	6	8
\mathbf{k} -grid				\mathbf{k} -grid		
2×2×2	-0.031	0.003	0.005	2×2×2	-0.088	-0.002
4×4×4	-0.035	0.000	0.002	4×4×4	-0.059	0.000

Table 5.1: The change in lattice constant a with respect to the value with $\text{rgkmax}=8$ and \mathbf{k} -grid=4×4×4 for two examples of clathrates.

Taking the relaxed structures obtained by these atom relaxations, the maximum forces F are calculated by performing a single GS calculation with $\mathbf{k}\text{-grid}=4\times4\times4$ and $\mathbf{rgkmax}=8$ without relaxation. The difference

$$\Delta F = F_{\text{relax}} - F_{\text{relax}}^{\text{REF}} \quad (5.3)$$

is presented in the left part of Tab. (5.2). The maximum force for different \mathbf{rgkmax} values but for the same $\mathbf{k}\text{-grid}$ hardly changes, whereas they change significantly by going from a $2\times2\times2$ $\mathbf{k}\text{-grid}$ to a $4\times4\times4$ $\mathbf{k}\text{-grid}$ at a fixed \mathbf{rgkmax} . Regarding $\mathbf{k}\text{-grid}=4\times4\times4$ and $\mathbf{k}\text{-grid}=6\times6\times6$, the difference of the maximum forces is small (below $0.1 \text{ mRy}/a_B$).

Furthermore, the energies of the GS calculations E_{relax} using the relaxed structures from atom relaxations with different parameters are considered. Their change

$$\Delta E_{\text{relax}} = E_{\text{relax}} - E_{\text{relax}}^{\text{REF}} \quad (5.4)$$

with respect to the energy E^{REF} of the reference GS calculation ($\mathbf{k}\text{-grid}=4\times4\times4$ and $\mathbf{rgkmax}=8$) is presented in the right part of Tab. (5.2). All energy differences are well below the needed accuracy of $1 \text{ meV}/\text{atom}$ (around $0.3 \text{ meV}/\text{atom}$), whereas the $\mathbf{k}\text{-grid}$ mostly influences this difference.

Due to the $\mathbf{k}\text{-grid}$ dependence of the force and the energy differences, the atom relaxation is performed with a fine $\mathbf{k}\text{-grid}=4\times4\times4$ and $\mathbf{rgkmax}=6$. This is enough to ensure that the force components are below the threshold $2.5 \text{ mRy}/a_B$ in the final GS calculation.

Ba ($x=10$)						
ΔF [mRy/ a_B]			ΔE_{relax} [meV/atom]			
$\mathbf{k}\text{-grid} \backslash \mathbf{rgkmax}$	6	8	$\mathbf{k}\text{-grid} \backslash \mathbf{rgkmax}$	6	8	
$2\times2\times2$	2.45	2.40	$2\times2\times2$	0.24	0.28	
$4\times4\times4$	0.09	0.00	$4\times4\times4$	0.05	0.00	
$6\times6\times6$	0.02		$6\times6\times6$	0.045		
Sr ($x=15$)						
ΔF [mRy/ a_B]			ΔE_{relax} [meV/atom]			
$\mathbf{k}\text{-grid} \backslash \mathbf{rgkmax}$	6	8	$\mathbf{k}\text{-grid} \backslash \mathbf{rgkmax}$	6	8	
$2\times2\times2$	1.34	1.17	$2\times2\times2$	0.10	0.11	
$4\times4\times4$	0.09	0.00	$4\times4\times4$	0.02	0.00	

Table 5.2: Atom relaxation: Convergence test of forces and energies with respect to different $\mathbf{k}\text{-grids}$ and \mathbf{rgkmax} values for two examples of clathrates.

5.2 Ground-state calculations

In order to make statements regarding the structural stability of the configurations, the energy differences of the structures at a fixed concentration have to be well converged with respect to the simulation parameters.

In Tab. (5.3), the energy differences of six structures of the Ba clathrate (with $x = 14$) labeled with 1, 2, \dots , 6 with respect to the GS (configuration 1) are shown for

different **k**-grids with fixed **rgkmax**=8 as well as for different **rgkmax**'s with a fixed **k-grid**=4×4×4. The energy differences for a rough **k-grid** are about 0.5 meV/atom smaller than the differences with a fine **k-grid**. Going from a 4×4×4 **k-grid** to a 6×6×6 **k-mesh**, the energy differences change less than 0.03 meV/atom. Calculations with **rgkmax**=8 lead to energy differences converged below 0.02 meV/atom, whereas the energy differences with **rgkmax**=6 are about 0.2 meV/atom larger than the converged values. For both convergence tests, the ordering of structures with their energy is the same for all the combinations of parameters. In Tab. (5.3), also the number of Al-Al bonds in the structures is indicated. The energy difference scales roughly linearly with the number of Al-Al bonds: each Al-Al bond increases the energy by about 7-10 meV/atom. If no Al-Al bonds are present, the energy of the structures differ by less than 1 meV/atom. This fact emphasizes the required accuracy of the energy difference below 1 meV/atom. Similar features are revealed in the convergences tests for the Sr clathrate, Tab. (5.4). From this analysis, it follows that in order to guarantee convergence below the 1 meV/atom threshold for the full composition range, a large **rgkmax** of 8 and a fine **k-grid** of 4×4×4 for the GS calculation suffices.

The definition of the radial orbitals inside the MTs influence the accuracy of the DFT calculation. The energy parameters (see Sec. 4.2), which ultimately affect the shape of the radial orbitals, are kept fixed for all compositions. That means that a change in the on-site Madelung potential with the composition leads to a slight disalignment between the eigenvalues and the linearization energies. However, by augmenting the flexibility of the basis inside the spheres with additional local orbitals, this problem is highly alleviated. Therefore, it is possible to use the same species configurations for each composition and still assure good convergence of the valence electrons treated in a scalar-relativistic manner (option *iora** in **exciting**).

In Table (5.5), the parameters used for structure optimization and the GS calculation are summarized. The usual procedure for a full *ab-initio* calculation consists of typically two cycles with a consecutive cell and atom relaxation. The structure

ΔE [meV/atom] for Ba ($x=14$, LDA)						
Configuration	1	2	3	4	5	6
#Al-Al bonds	0	0	0	1	2	6
rgkmax =8						
k-grid						
2×2×2	0	0.225	0.365	7.086	17.35	45.74
4×4×4	0	0.780	0.973	7.415	17.81	46.81
6×6×6	0	0.715	0.972	7.478	17.79	46.85
k-grid =4×4×4						
rgkmax						
6	0	0.956	1.120	7.526	17.83	47.03
8	0	0.780	0.959	7.415	17.81	46.81
9	0	0.794	0.986	7.414	17.79	46.80

Table 5.3: Convergence test of energy differences for 6 structures of the same composition exemplarily for the Ba clathrate ($x=14$, LDA). In the upper part, the **k-mesh** is varied, in the lower part the value of **rgkmax**.

ΔE [meV/atom] for Sr ($x=10$, PBEsol)			
Configuration	1	2	3
#Al-Al bonds	0	1	3
rgkmax=8			
k-grid			
2×2×2	0	12.50	34.50
4×4×4	0	13.62	35.88
6×6×6	0	13.74	36.07
k-grid=4×4×4			
rgkmax			
6	0	13.90	35.64
8	0	13.62	35.88

Table 5.4: Convergence test of energy differences for different structures of the same composition exemplarily for the Sr clathrate ($x=10$, PBEsol). In the upper part, the **k-mesh** is varied, in the lower part the value of **rgkmax**.

optimization is considered as completed, if the lattice constant a_0 does not change with respect to the a_0 from a previous cell relaxation or if the atom positions remain unchanged in the atom relaxation.

	k-grid	rgkmax	Convergence criteria
Cell relaxation	2×2×2	8	$E_{\text{tol}}(\text{guide})=0.2$ meV, $\Delta E_{\text{tol}}=0.2$ meV, $N_{\text{runs}} \geq 6$
Atom relaxation	4×4×4	6	$F_{\text{tol}} = 2$ mRy/atom ($E_{\text{tol}}=1.4$ meV)
Ground state	4×4×4	8	$E_{\text{tol}} = 0.5$ meV

Table 5.5: Parameters for the structure relaxation and the ground-state calculations to obtain the *ab-initio* energy.

6 Ground-state configurations

The iterative procedure of the code **CELL** is used to explore the configuration space and to determine the GS configurations of the clathrate compounds $\text{Ba}_8\text{Al}_x\text{Si}_{46-x}$ and $\text{Sr}_8\text{Al}_x\text{Si}_{46-x}$ in the composition range $6 \leq x \leq 16$. In Sec. 6.1, the iterative GS search (GSS) with **CELL** is presented in detail exemplarily for the Ba clathrate. The ground-state configurations of both clathrate compounds obtained from the GSS are discussed in Sec. 6.2.

6.1 Ground-state search

As an example, a detailed description of the GSS for the clathrate compound $\text{Ba}_8\text{Al}_x\text{Si}_{46-x}$ with the CE technique is presented.

At first, an overview is given regarding the CE construction and the choice of the optimal set of clusters of the CE, which gives the lowest CV. To find the optimal set of clusters, least-squares fits for different sets of clusters are executed. The set of clusters is defined by two parameters, the maximal number of points building the cluster, N_{points} , and the radius r up to which the clusters are considered (Sec. 3.3). The total number of clusters corresponding to a certain choice of these parameters is presented in Tab. (6.1). All possible sets up to the cluster size $r \leq 4$ are shown, which include all nearest- and next-nearest-neighbor atoms. The empty cluster and the three different 1-point clusters representing the three Wyckoff positions $24k$, $16i$,

No. of clusters up to N_{points}				
r [Å]	N_{points}	2	3	4
2.2440		5	-	-
2.3771		6	-	-
2.4204		7	-	-
2.6064		8	-	-
3.8179		9	10	-
3.8850		10	14	-
3.8853		11	19	22
3.9030		12	23	27
3.9789		14	27	34

Table 6.1: Size of the sets of clusters specified by the maximum radius r and the maximum number of points, N_{points} , building the cluster.

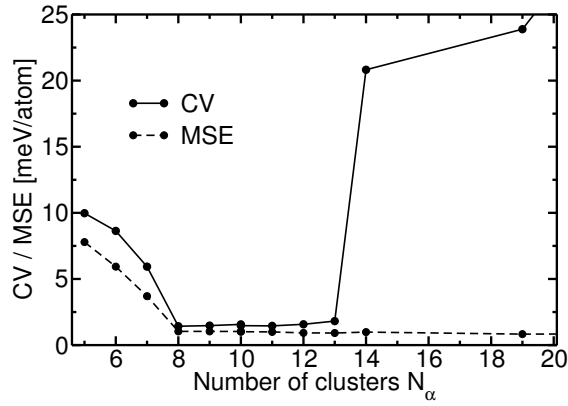


Figure 6.1: Diagram of the change in CV and MSE with the number of clusters.

and $6c$ of the host structure ($r = 0$) are always included.

An example of the change of the LOO-CV, here simply called CV, and the MSE with increasing number of clusters, N_α , is shown in Fig. 6.1. This plot is based on a large set of *ab-initio* data ($N_s = 35$). With the increase of N_α , CV and MSE decrease until the optimal set of clusters is reached (in this case $N_{\text{points}} = 8$ with up to 2-point clusters). Here, the MSE is slightly lower than the CV. It follows a range where additional clusters do not lead to an improvement in the CV but a slight increase. However, the MSE in this range still decreases. Far away from the optimal choice of clusters the CV jumps abruptly to significantly larger values whereas the MSE is further reduced. The monotonic decrease of the MSE indicates an improved fitting to the *ab-initio* data, though the predictive power of the CE (indicated by the CV) deteriorates with further increase of the number of clusters.

The GSS is done with the iterative procedure of **CELL**, introduced already in the workflow of Fig. 3.1 (b). Figure 6.2 shows different stages of the GSS. Detailed information about the CE for each iteration in the GSS is listed in Tab. (6.2). The labeling in the plots is as follows: The *ab-initio* energies are shown as circles, whereas the CE energies are represented by dots. The predicted energies of the structures visited by the Metropolis sampling (MS) are represented by the blue dots. In addition, each iteration of the CE construction is indicated by a different color. On the y axis of the GSS plots, the energy of mixing is depicted, defined as

$$e_{\text{mix}}(x) = \frac{E_{a.i.}(x) - \left[\hat{E}_{\text{CE}}(\text{Ba}_8\text{Si}_{46}) + \left(\hat{E}_{\text{CE}}(\text{Ba}_8\text{Al}_{46}) - \hat{E}_{\text{CE}}(\text{Ba}_8\text{Si}_{46}) \right) x/46 \right]}{N_{\text{atoms}}}. \quad (6.1)$$

The energy of mixing represents the energy difference between the *ab-initio* energy ($E_{a.i.}$) and the energy obtained from a linear interpolation between the predicted energies of the pristine structures, $\text{Ba}_8\text{Si}_{46}$ and $\text{Ba}_8\text{Al}_{46}$, calculated using the CE from the last iteration (iteration 5 in Fig. 6.2). The energy given by the linear interpolation can be considered as a reference energy. For $x = 0$ and $x = 46$, the predicted energy of mixing is zero.

At the beginning of the GSS, the *ab-initio* energies for the initial set of random structures are calculated (gray circles in Fig. 6.2(a)) and a CE is constructed from them. For this CE, a set of 8 clusters up to 2-point clusters with a CV of around 10 meV/atom and a MSE of 2.3 meV/atom (see Tab. (6.2)) is the optimal choice. With this CE, the MS (blue dots) predicts new lowest non-degenerate structures

Iteration	N_s	N_α	N_{points}	A	LOO-CV [meV/atom]	MSE [meV/atom]
1	12	8	2	-	9.94	2.34
2	22	11	2	-	4.68	3.08
3	32	10	3	-	3.77	1.98
4	43	16	2	-	3.36	3.35
5	48	22	2	-	3.31	1.32
6 CE1	35	8	2	-	1.35	1.12
6 CE2	23	9	3	-	2.06	1.04
7 CE1	35	8	2	10^{-6}	1.43	1.04
7 CE2	23	9	3	0.02	1.02	0.75

Table 6.2: Parameters determining the CE of each iteration. After five iterations, the compositional range is split into two ranges (see description below). N_s indicates the number of structures used for the CE construction, A is the penalization value (see Sec. 3.2).

for each composition which form the set of structures for iteration 1 (dark red dots in Fig. 6.2 (a)). The MS is performed for each composition and samples until no new lowest-non-degenerate configuration is found after $N_{\text{sampl}} = 100000$ sampling steps from the last accepted one. Thus, in total, typically 103000 configurations are sampled for each composition x . In most cases the Boltzmann distribution with a temperature of $T = 1000K$ is used for the MS to ensure that the system can also cross energy barriers in the configuration space. For the composition with $x = 10$, the MS yields new structures only inside a small energy range, as compared to other compositions, and the energy of the predicted GS is still close to the $E_{a.i.}$ of the random structure.

In the next step, the *ab-initio* energies of iteration 1 are calculated (red circles in Fig. 6.2 (b)), and they are similar to their predicted values from the initial CE (red dots). Figure 6.2 (b) reveals a slightly better agreement of the predicted energies with the initial set (training set) than with the set of iteration 1. This results from the fact that the initial set is used to construct the CE. Deviations of the predicted energies from *ab-initio* energies are quantified by the MSE. For the set of iteration 1, they are estimated from the CV since the data is not included in the CE construction. As shown in Tab. (6.2), the MSE is about five times smaller than the CV.

Once a new set of structures along with their *ab-initio* energies is obtained, it can be included in the construction of a new CE to improve its predictability. The predictive power improves with the number of *ab-initio* data. Furthermore, a large set of *ab-initio* energies makes a fit to a larger set of interactions possible. In Table (6.2), the CV and the MSE clearly decrease with each iteration. For the next iterations, 2 (yellow) and 3 (green), the procedure is similar as in Figs. 6.2 (a) and (b).

In iteration 4, shown in Fig. 6.2 (c), the optimal CE with now 16 clusters predicts new lowest-non-degenerate structures (violet dots connected with a violet dashed line). Only the *ab-initio* energies of new GSs suggested by the CE are calculated from this new set of structures. Figure 6.2 (d) shows the GSS plot with the new *ab-initio* energies of iteration 5. Except for $x = 13$, the difference to the predicted CE

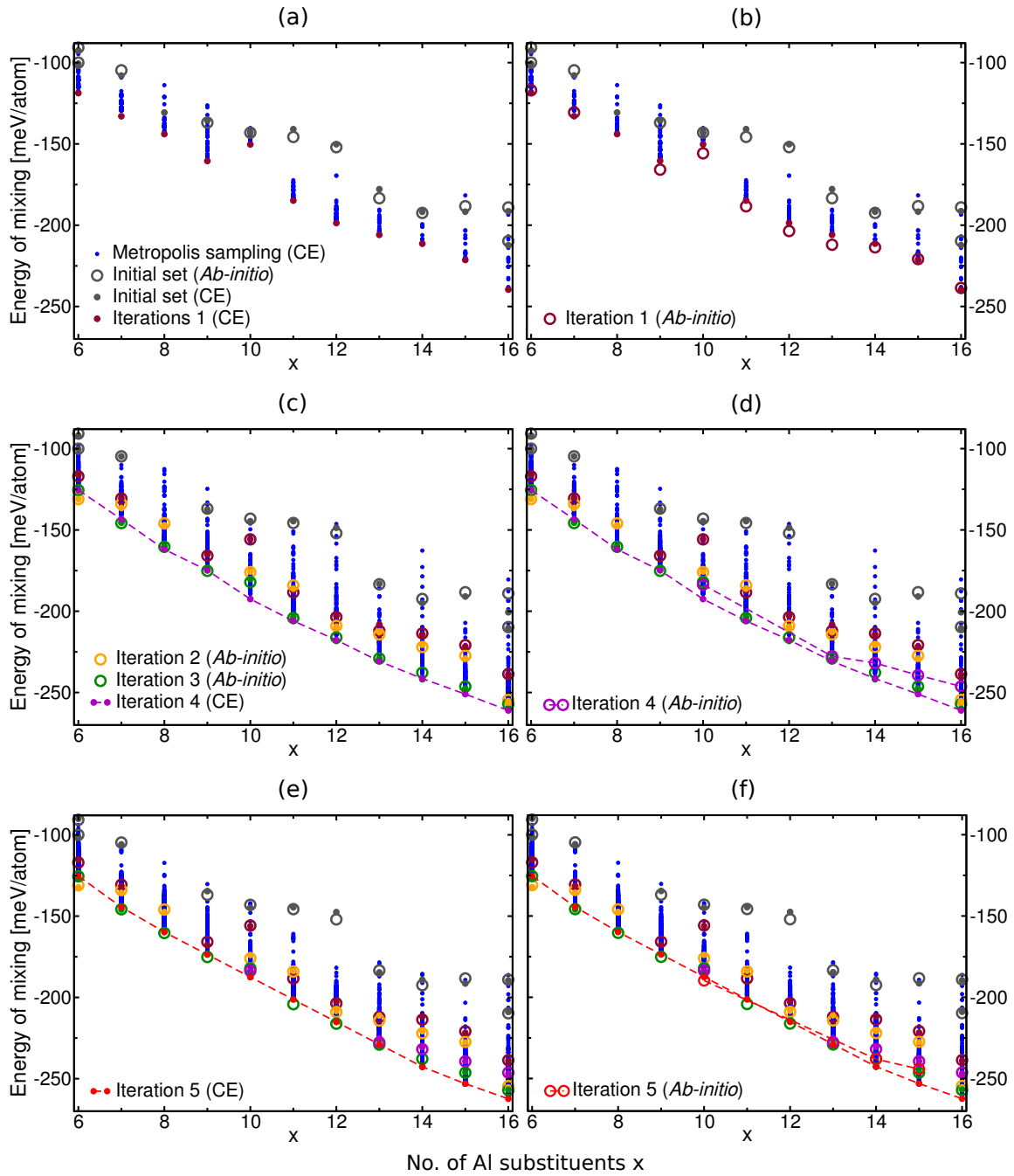


Figure 6.2: Successive steps of a GSS with **CELL**: Circles indicate *ab-initio* energies, dots represent predicted energies from the CE. The CE energies of structures visited by the MS are represented by the blue dots. For each iteration a different color is used.

energy (around 10 meV/atom) is much larger than the CV (around 3.5 meV/atom). After another iteration including the *ab-initio* energies of structures of iteration 5 (Fig. 6.2 (e)), the optimal CE with now 22 clusters leads to a good prediction of the energies of iteration 5. But again, the new set of lowest-non-degenerate structures (indicated with red dots connected with a red dashed line) reveal still a difference between the CE prediction and the *ab-initio* energy (Fig. 6.2 (f)), larger than the CV.

Discrepancies between the predictions and the *ab-initio* energies can result from

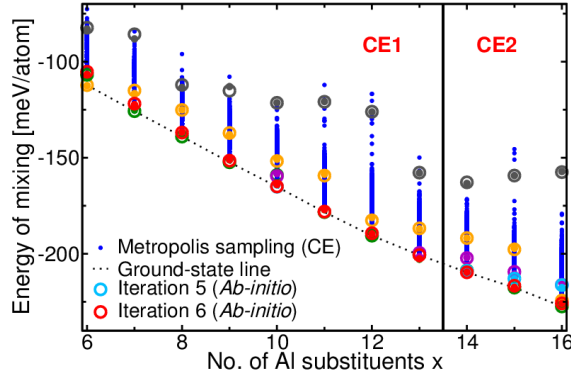


Figure 6.3: The GSS for $\text{Ba}_8\text{Al}_x\text{Si}_{46-x}$ with iteration 6 as the last iteration. Two separate CEs are performed: CE1 in the range $x \in [6, 13]$ and CE2 in the range $x \in [13, 16]$.

overfitting. In this case, the CV indicates a too large set of clusters to be optimal. As regards the clusters used to construct the CE, their associated ECIs are very small for clusters beyond the nearest neighbors and below the accuracy of the *ab-initio* data. Additionally, physical intuition would suggest a decrease of the interaction strength with the increase of the radius of the related cluster. However, in our case this is not maintained for a large set of clusters as 16 or 22 clusters. A solution for this problem is provided by the penalization term in Eq. (3.9) (Sec. 3.2). This penalization is applied to the interactions of a set of clusters considered as physically relevant. The change of the interactions upon addition of new clusters to the CE and the influence of penalizing them is discussed at the end of this section.

Another reason for the failure of the CE predictions can be a significant change in the configurational dependence of the energy over the composition range $x \in [6, 16]$. Here, the predictions of the CE fail when the number of substituents is large ($x \geq 13$). Taking into account that most of the data used to build the CE comes from the lower range $x < 13$, this could indicate that the physical interactions are intrinsically different for small and large Al content. This assumption is strengthened by inspecting the density of states at the Fermi level, $\text{DOS}(E_F)$ (discussed in more detail in Sec. 7.1). The $\text{DOS}(E_F)$ decreases with the number of Al substituents, but slightly increases again around $x = 13-14$. Thereafter, it goes down again until it becomes zero or close to zero at the Zintl composition. Considering this behavior and the failure of the CE when applied to the entire composition range, suggests to perform separate CEs for two ranges of Al content.

The CE constructed from the *ab-initio* data of the first range $x \in [6, 13]$ is labeled CE1, whereas the CE based on the *ab-initio* data of the second range $x \in [14, 16]$ is labeled CE2. Fig. 6.3 shows the GSS plot concerning iteration 6 with the new lowest-non-degenerate states obtained from different CEs (here now in red, whereas iteration 5 is in light blue). The energy of mixing here is calculated using both CEs. From the CE1, the energy of the pristine structure $\text{Ba}_8\text{Si}_{46}$ is obtained, and from CE2 the energy of $\text{Ba}_8\text{Al}_{46}$. In some cases, the MS with the improved CE does not yield a new GS for a given composition and proposes a configuration with an energy close to the GS energy (next lowest-non-degenerate structure). Nevertheless, this new structure can be also useful to improve the CE. In iteration 6, the *ab-initio* energies of the complete set of structures are calculated to verify the approach of separate CEs. They are in good agreement with the predictions in both ranges.

Again, the optimal CE1 and CE2 consist of a small set of clusters with $N_\alpha = 8$. The interaction parameters for the different composition ranges will be discussed in the next section. The black dashed line connects the GS energies for each composition. For clathrates with a large Al content, the GS line slightly departs from its almost linear decrease with respect to x for $x \leq 12$, and presents an inflection point around $x = 14$.

The CEs of the GSS (Fig. 6.3) can be used to predict different properties of the clathrates. The occupation factors (OF) of the three Wyckoff positions are shown and discussed in detail in Sec. 7.2.3, Fig. 7.8. They reveal an abrupt change for the $24k$ and $16i$ sites and a crossing of them just at the splitting point between $x = 13$ -14. In order to ensure that this behavior is physical, and not an artifact of the separation, the following questions have to be clarified: Is the separation of the composition range made at the right position? Does the prediction improve if the two ranges are chosen in a different way? To this extent, we perform CEs based on different sets of *ab-initio* data for the lower and the upper range. For the lower range, CEs with x between 6 and 12 and between 6 and 14 are performed, whereas for the upper range, we choose CEs with x between 12 and 15 and between 13 and 16. In doing so, an overlap between the two ranges is possible. This overlap could lead to a smooth transition of the OFs. It turns out that the inclusion of data from $x = 14$ for low x does not affect the predictability of CE1 in the range of $x \in [6, 13]$ but leads to wrong predictions at $x = 14$. Wrong predictions means especially that the ordering of the *ab-initio* energies is not captured by the CE1. For high x , the inclusion of $x = 12$ leads to wrong predictions at $x = 12, 13$, and 14. In contrast, using the ranges $x \in [6, 13]$ and $x \in [13, 16]$, corresponding CEs, CE1 and CE2, lead to good predictions, also in the region close to the splitting point $x = 13$. These two CEs are used to perform iteration 7 of the GSS, which is illustrated in Fig. 6.4. In this figure, the black solid line indicates the starting point of the CE2 and the black dashed line the end of CE2. For the predictions of the overlap region, $x = 13$, the CE2 is chosen for predictions. CE1 has a CV around 1.4 meV/atom, and CE2 a value around 1.02 meV/atom. The OFs of the $24k$ and $16i$ sites still reveal a crossing between $x = 13$ -14, so we confirm this to be a physical effect rather than an artifact.

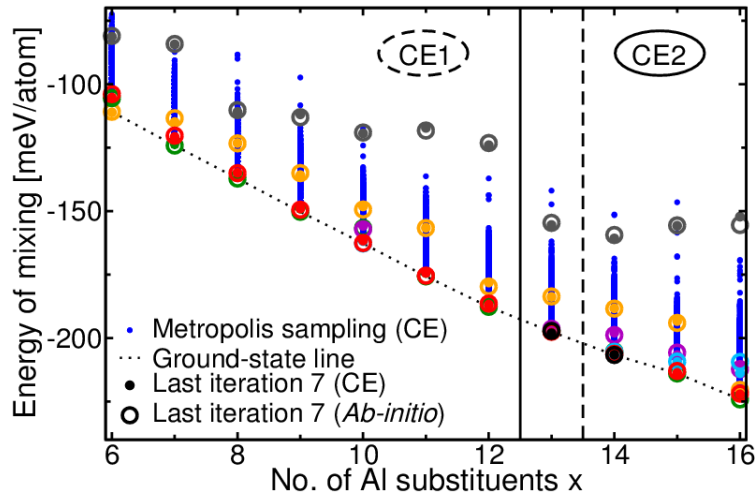


Figure 6.4: Final result of the GSS for $\text{Ba}_8\text{Al}_x\text{Si}_{46-x}$ (LDA). Two CEs are performed: CE1 in the range $x \in [6, 13]$ and CE2 in the range $x \in [13, 16]$. CE1 and CE2 have an overlap at $x = 13$.

For all further considerations, we use the above described CEs with the overlap at $x = 13$.

At this point, we take a closer look at how the interaction strength of the clusters changes with respect to the number of clusters included in the CE. Figure 6.5 illustrates the change of the interactions with respect to the number of clusters, N_α , used to construct the CE. It is performed with penalization of $A = 0.001$ applied to the ECIs. Different kinds of N_{points} -point clusters are considered. N_{points} and the corresponding radii are the same as in Tab. (6.1). The first four 2-point clusters (up to $N_{\text{points}} = 8$) represent the nearest neighbor interactions with a radius below 2.6 \AA . The next clusters (beginning with $N_{\text{points}} = 9$) have larger radii with sizes from $r \approx 3.56 \text{ \AA}$ onwards. Thus, it is reasonable that the magnitude of the next-nearest neighbor interactions is much smaller. These interactions are well above the accuracy of *ab-initio* data (dashed black line), whereas the additional interactions are below this threshold. If a set of clusters with small interactions is added to the CE this can lead to an abrupt change of the iteration strength of the nearest-neighbor iterations. For instance at $N_\alpha = 14$, a few 3-point clusters with small negative interactions are added. In this case, the k - k iteration jumps to a value that is 50 meV larger. Thus, many small interactions can spoil the large interactions. Furthermore, it is questionable if the inclusion of next-nearest-neighbor clusters captures any physical relevant interactions, since their value can flip from positive to negative by adding new clusters. In the case of $N_\alpha = 10$ (Fig. 6.5, right), the 3-point clusters have positive interactions, whereas the interactions of the 3-point clusters at $N_\alpha = 14$ are all negative. Due to the fluctuations of these small interactions, they spoil the predictability of the CE rather than leading to an improvement.

Usually, the CV reaches its minimum at $N_\alpha = 8$, as seen in Fig. 6.1. This means that a small set of clusters with $N_\alpha = 8$ is appropriate to describe the interactions of the clathrate structures. In some CEs, a set of up to $N_\alpha = 10$ clusters is used since the additional clusters reduce the CV slightly and do not spoil the predictability of the CE.

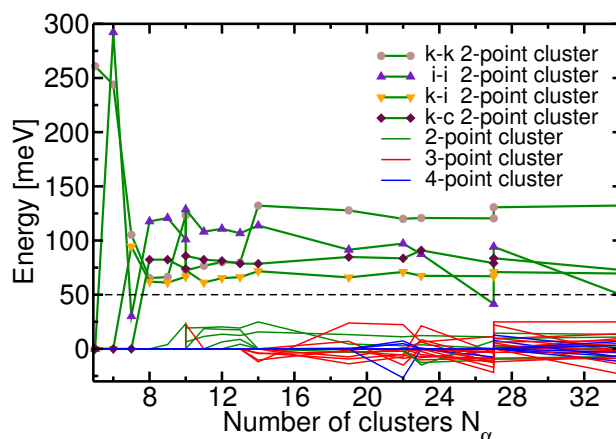


Figure 6.5: Interaction parameters in meV as a function of the number clusters N_α considered in the CE with penalization $A = 0.001$. The black line indicates the accuracy of the *ab-initio* data.

6.2 Results of ground-state searches for all clathrates

With the CE approach, the clathrate structures $\text{Ba}_8\text{Al}_x\text{Si}_{46-x}$ and $\text{Sr}_8\text{Al}_x\text{Si}_{46-x}$ are investigated with two different exchange-correlation functionals, LDA and PBEsol.

At this point, the LDA result of the GSS for $\text{Sr}_8\text{Al}_x\text{Si}_{46-x}$, illustrated in Fig. 6.6, is briefly discussed. It is performed in the same way as for $\text{Ba}_8\text{Al}_x\text{Si}_{46-x}$. The $\text{DOS}(E_F)$ (see Sec. 7.1) shows a similar feature around $x = 13$ -14. Consequently, two CEs are performed with an overlap at $x = 13$, in the same way as in the case of the Ba clathrate. At $x = 13$, the CE1 is chosen for predictions. Similar to the Ba clathrate, the GS energy decreases linearly with the number of substituents below $x \leq 12$ and presents an inflection point at $x = 14$. The results of of this GSS are discussed together with all GSSs in the following paragraphs. The black vertical line defines the CE used for describing the system. Below this line CE1 is used, above CE2 is used. This is valid for all GSS plots. The GSS plots based on the exchange functional PBEsol are shown in the appendix, Sec. A.2.

Table (6.3) provides a summary of the final CEs for both clathrates. Their LOO-CVs are below 2 meV/atom, except for the Sr clathrate with the PBEsol functional. The LMO-CV is calculated with 90% of the *ab-initio* data as construction set and 10% as the validation set. It is always slightly higher than the LOO-CV. However, in all CEs the LMO-CV leads to the same optimal set of clusters as the LOO-CV. The penalization applied to the interactions is usually very small. The important advantage of the penalizations is that it avoids the invertibility problem explained in Sec. 3.2.

The CEs mainly consist of $N_{\text{points}} = 8$ clusters. The empty cluster J_0 and the three 1-point clusters J_k , J_i , and J_c arising from the three Wyckoff positions have a zero radius. The additional clusters are illustrated in Fig. 6.7. The atoms of the host structure are shown in yellow, the guest atoms in gray. Big atoms encircled by a black ellipse represent a cluster. Regarding the color code, green is always used for the $24k$, blue for the $16i$, and red for the $6c$ position. There are four different nearest-neighbor clusters possible due to the bondings of the host atoms, as seen in

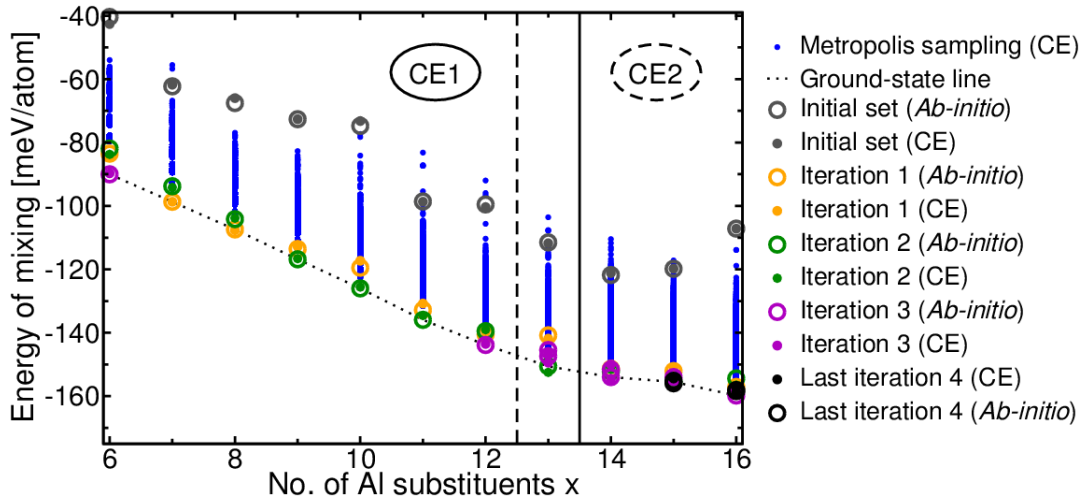


Figure 6.6: Final result of the GSS for $\text{Sr}_8\text{Al}_x\text{Si}_{46-x}$ (LDA). Two CEs are performed: CE1 in the range $x \in [6, 13]$ and CE2 in the range $x \in [13, 16]$. CE1 and CE2 have an overlap at $x = 13$.

		Ba		Sr	
CE1		LDA	PBEsol	LDA	PBEsol
N_s		35	25	28	25
N_α		8	8	8	8
N_{points}		2	2	2	2
A		10^{-6}	0.02	0.005	10^{-6}
$J(0)-J(0, \text{CE1})$	[meV]	0	0	0	0
$J(k)-J(c)$	[meV]	37.1	108.2	120.6	135.1
$J(i)-J(c)$	[meV]	121.7	159.7	136.7	159.6
$J(c)-J(c)$	[meV]	0	0	0	0
$J(k-k)$	[meV]	45.7	66.5	66.2	69.5
$J(i-i)$	[meV]	114.0	87.1	73.9	75.0
$J(k-i)$	[meV]	62.2	61.2	53.5	50.0
$J(k-c)$	[meV]	84.3	70.6	64.8	58.8
$J(k-_-i)$	[meV]	-	-	-	-
$J(k-k-i)$	[meV]	-	-	-	-
LOO-CV	[meV/atom]	1.43	0.96	1.44	3.83
LMO-CV[10%]	[meV/atom]	1.62	1.07	1.80	4.18
MSE	[meV/atom]	1.04	0.73	1.17	1.47
CE2		LDA	PBEsol	LDA	PBEsol
N_s		23	17	18	19
N_α		10	10	8	8
N_{points}		3	3	2	2
A		0.02	0.1	0.001	0.1
$J(0)-J(0, \text{CE1})$	[meV]	2.6	2.8	1.2	1.8
$J(k)-J(c)$	[meV]	106.3	126.1	73.7	103.4
$J(i)-J(c)$	[meV]	163.0	235.1	130.0	153.8
$J(c)-J(c)$	[meV]	0	0	0	0
$J(k-k)$	[meV]	81.2	48.2	37.8	30.4
$J(i-i)$	[meV]	94.7	99.8	83.5	50.9
$J(k-i)$	[meV]	73.2	79.5	40.3	55.8
$J(k-c)$	[meV]	69.0	64.2	65.2	60.8
$J(k-_-i)$	[meV]	0	0	-	-
$J(k-k-i)$	[meV]	3.4	0.3	-	-
LOO-CV	[meV/atom]	1.20	0.56	1.80	2.08
LMO-CV[10%]	[meV/atom]	1.26	0.62	2.00	2.40
MSE	[meV/atom]	0.75	0.51	0.96	1.74

Table 6.3: Parameters of the CEs for each GSS and the quality of the CE indicated by the MSE and CV.

Fig. 2.2: $k-k$, $k-i$, $k-c$ and $i-i$ (encircled with black solid lines in Fig. 6.7). Each of them builds a 2-point cluster. In some CEs, a set of 10 clusters is chosen, where the additional clusters have very small interactions. One of them is a 2-point cluster, which joins the next-nearest-neighbors of the i and k sides, represented with $k-_-i$. If the k site between these k and i sites is included in the cluster, it forms a 3-point cluster $k-k-i$ (encircled with the black dashed line in Fig. 6.7).

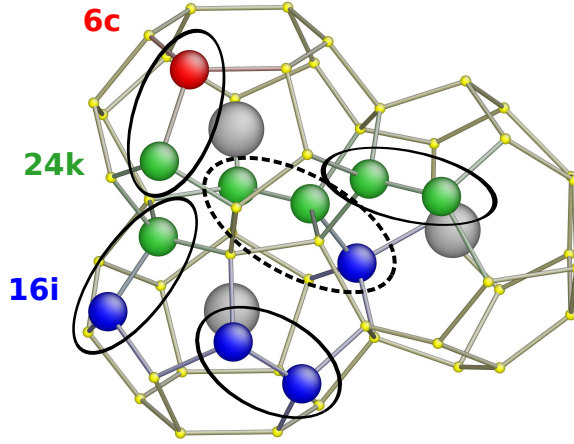


Figure 6.7: Clusters of the CE for clathrates. Guest atoms in gray, host structures in yellow. Big atoms in the host structure encircled by a black ellipse build a cluster. The Wyckoff positions are represented by different colors: 24k - green, 16i - blue, 6c - red.

Taking a closer look at the interaction strength, the interaction of the empty cluster in the CE2 is larger than in the CE1. Furthermore, the differences of the 1-point clusters with respect to J_c are slightly smaller in CE1 than in CE2 for the Ba clathrates, but similar in the case of Sr. The ordering of the 1-point clusters is independent of the type of guest atoms inside the clathrate structure and, moreover, independent of the composition range. In each CE, the smallest interaction is J_c , and the largest J_i , with J_k in between.

In order to obtain a physical interpretation of the ECIs, the energy differences between *ab-initio* calculations are analyzed (see Tab. (6.4)). The configurations are presented by the notation “ $(k, i, c) N_b$ ”, where k , i , and c indicate the number of Al atoms sitting at the k , i and c site, respectively, and N_b indicates the number of Al-Al bonds (trivalent bonds) in the structure. Now, if an Al atom at the site v is added, the change ΔE in the predicted energy can be approximated by using only the empty and 1-point clusters as

$$E[(k+1, i, c) 0] - E[(k, i, c) 0] = 2 J_k \quad \text{if } v = k \quad (6.2)$$

$$E[(k, i+1, c) 0] - E[(k, i, c) 0] = 2 J_i \quad \text{if } v = i \quad (6.3)$$

$$E[(k, i, c+1) 0] - E[(k, i, c) 0] = 2 J_c \quad \text{if } v = c . \quad (6.4)$$

These energy differences result from removing one Si atom at v with the energy contribution $-J_v$ and inserting one Al atom with a contribution $+J_v$ (occupancy variable $\sigma = 1$ for an Al atom) at this position. The energy changes upon swapping a pair of Al and Si atoms at the sites k and c or k and i are, respectively,

$$E[(k, i, c) 0] - E[(k+1, i, c-1) 0] \simeq 2(J_c - J_k), \quad (6.5)$$

$$E[(k, i, c) 0] - E[(k+1, i-1, c) 0] \simeq 2(J_i - J_k). \quad (6.6)$$

From the *ab-initio* energies of the Ba clathrate compounds with $x = 6$ and $x = 16$, the energy differences $\Delta E_{a.i.}$ of different configurations are shown in Tab. (6.4). Using Eq. (6.5) and Eq. (6.6) with the ECIs taken from the CE for the Ba clathrate

$\Delta E = E(y) - E(y_0)$	$\Delta E_{a.i.}$	$\Delta \hat{E}_{\text{CE}}$	$\Delta \hat{E}_{\text{CE}}$	$ \Delta E_{a.i.} - \Delta \hat{E}_{\text{CE}} $
$y = (k, i, c) N_b$	[meV]	$N_{\text{points}} = 1$ [meV]	$N_{\text{points}} = 2$ [meV]	$N_{\text{points}} = 2$ [meV/atom]
$x = 6, y_0 = (1, 0, 5) 0$				
(0,0,6) 0	-290.5	-74.2	-239.8	0.94
(1,0,5) 0	0	-	-	-
(0,1,5) 0	85.0	169.2	76.8	0.15
(4,1,1) 1	1323			
$x = 6, y_0 = (11, 2, 3) 0$				
(12,1,3) 0	-86.5	-113.4	-77.8	0.16
(11,2,3) 0	0	-	-	-
(10,3,3) 0	79.9	113.4	77.8	0.04
(6,6,4) 0	220.9			
(6,6,4) 2	521.0			

Table 6.4: Estimates of the energy differences using the interactions of the CEs. A model with up to the nearest-neighbor interactions gives a good agreement with the energy differences of the *ab-initio* calculations.

(LDA) in Tab. (6.3), the predicted energies $\Delta \hat{E}_{\text{CE}}$ are obtained (see column indicated with $N_{\text{points}} = 1$ in Tab. (6.4)). These differ from their *ab-initio* counterparts $\Delta E_{a.i.}$. However, it can be concluded that J_c has to be smaller than the J_k and, furthermore, J_k has to be smaller than J_i allowing already for a first interpretation of the 1-point ECIs, whose ordering indicate preferred occupancies.

These estimates come closer to the *ab-initio* energies, if the nearest-neighbor interactions are included ($N_{\text{points}} = 2$). Under the assumption that there are no Al-Al bonds involved in the reconfiguration of the structure, the predictions of the previous energy differences are improved as follows:

$$E[(k, i, c) 0] - E[(k + 1, i, c - 1) 0] \simeq 2 (J_c - J_k) + 2 (J_{kk} + 2J_{ki} - 3J_{kc}), \quad (6.7)$$

$$E[(k, i, c) 0] - E[(k + 1, i - 1, c) 0] \simeq 2 (J_i - J_k) + 2 (J_{kk} - J_{ki} + J_{kc} - J_{ii}). \quad (6.8)$$

A simple interpretation of the two-point interaction strengths is not possible, since there are too many free parameters. Now, the agreement with the *ab-initio* results is much better and differs by less than 1 meV/atom (column $|\Delta E_{a.i.} - \Delta \hat{E}_{\text{CE}}|$). This is valid for $x = 6$, as well as for $x = 16$.

The site occupations and the number of Al-Al bonds (keeping the notation $(k, i, c) N_b$) as obtained from the two functionals, LDA and PBEsol, are listed in Tab. (6.5) for the GS configurations of the Ba and Sr clathrates. Due to the ordering $J_c < J_k < J_i$ of the 1-point interactions, the occupation of $24k$ sites is expected to be more likely than the occupation of the $16i$ sites. However, this is not the case, when the site occupations of the GS configurations are considered. At $x = 6$, the $6c$ site is fully occupied for both clathrate compositions. Adding an Al atom ($x = 7$) at the $24k$ would lead to a structure with Al-Al bonds, since every $24k$ site has one $6c$ site as neighbor. The energy differences between structures with and without Al-Al bonds are much larger than the differences resulting from only a change in the occupation of the Wyckoff sites with fixed number of Al-Al bonds. This is valid for the complete composition range. Some examples of the energy differences related to

a change in the number of Al-Al bonds are given in Tab. (6.4) for the configurations (4,1,1) 1 and (6,6,4) 2; and have already been seen in Tab. (5.3) and Tab. (5.4). Thus, the nearest-neighbor pair interactions prevent the occupation of the $24k$ site and cause an occupation of the $16i$ sites for low x . The $6c$ site is still preferred over the $24k$ and $16i$ sites.

In the middle of the composition range, $x = 10-14$, for the Ba clathrate, the preference of the $6c$ sites gets reduced and occupation of $24k$ and $16i$ sites occurs. These configurations still avoid Al-Al bonds. In some cases, the energies of a few lowest-non-degenerate structures are very close (energy difference below the accuracy of the *ab-initio* calculations) to the GS energy; their configurations are shown in Tab. (6.5) below the corresponding GS configuration. These states close to the GS clearly appear in the transition region where the $6c$ site gets less occupied and the k site becomes preferred over the i site.

For the Sr clathrate, the preference of the $6c$ site is kept even in the middle range. Avoidance of Al-Al bonds and keeping the full occupation of the $6c$ is possible until $x = 14$. At $x = 14$ the $16i$ site is half occupied and an additional Al atom at $16i$ would cause an Al-Al bond between two $16i$ sites. At $x = 15$, the GS configuration reveals one Al-Al bond. The next lowest-non-degenerate state has again no Al-Al bond, but pays the cost of having one atom less at the $6c$ sites.

For the Zintl composition ($x = 16$), the GS configuration for the Ba and the Sr clathrate is the same. It has a half occupation of the $6c$ and $24k$ sites, the

GS configuration $(k, i, c)N_b$				
x	Ba		Sr	
	LDA	PBEsol	LDA	PBEsol
6	(0,0,6) 0	(0,0,6) 0	(0,0,6) 0	(0,0,6) 0
7	(0,1,6) 0	(0,1,6) 0	(0,1,6) 0	(0,1,6) 0
8	(0,2,6) 0	(0,2,6) 0	(0,2,6) 0	(0,2,6) 0
9	(0,3,6) 0	(0,3,6) 0	(0,3,6) 0	(0,3,6) 0
10	(0,4,6) 0 (4,1,5) 0	(0,4,6) 0 (4,1,5) 0	(0,4,6) 0	(0,4,6) 0
11	(0,5,6) 0 (4,2,5) 0	(0,5,6) 0 (4,2,5) 0	(0,5,6) 0	(0,5,6) 0
12	(0,6,6) 0 (4,3,5) 0	(0,6,6) 0	(0,6,6) 0	(0,6,6) 0
13	(8,1,4) 0 (0,7,6) 0 (4,4,5) 0	(8,1,4) 0 (0,7,6) 0	(0,7,6) 0	(0,7,6) 0
14	(8,2,4) 0 (7,3,4) 0	(8,2,4) 0	(0,8,6) 0 (4,5,5) 0	(0,8,6) 0
15	(12,0,3) 0	(12,0,3) 0	(1,8,6) 1 (2,8,5) 0 (12,0,3) 0	(1,8,6) 1 (2,8,5) 0
16	(12,1,3) 0	(12,1,3) 0	(12,1,3) 0	(12,1,3) 0 (11,2,3) 0

Table 6.5: GS configurations of the clathrate compounds $\text{Ba}_8\text{Al}_x\text{Si}_{46-x}$ and $\text{Sr}_8\text{Al}_x\text{Si}_{46-x}$ obtained from GSS's with LDA and PBEsol.

remaining atom goes to the $16i$ site. Here, the preference of the $24k$ over the $16i$ site is maintained. The $6c$ site is less occupied to avoid Al-Al bonds. There exists also a structure without Al-Al bonds for the Zintl composition with 4 Al atoms at $6c$ instead of 3. However, this configuration having 6 Al atoms at $16i$ is significantly higher in energy than the GS.

The avoidance of trivalent bonds for clathrates with Ga and Ge atoms in the framework has been reported from DFT calculations [19]. In that work, nine different configurations of the Zintl composition were investigated, finding the $(12, 1, 3) 0$ configuration most favorable. With our CE technique, we find similar characteristics for the Al-Si based clathrates at the Zintl composition. It should be noted, though, that our method provides an enormously larger (and unbiased) search in compositional space.

From a general point of view, it must be stressed that in our work all GSSs are performed completely independently from each other. The GSS's for the two different exchange-correlation energy functionals lead to the same GS configurations, for both the Ba and Sr clathrates. This fact emphasizes the completeness of the GSS's for both clathrates and that the true GSs are found.

7 Clathrate properties

This chapter deals with the electronic and structural properties of the clathrate compounds. The discussion of the electronic properties (in Sec. 7.1) mainly focuses on the density of states (DOS). As structural properties, the lattice constants, bond distances, and occupancy factors are considered in Sec. 7.2.

7.1 Electronic properties

The free electrons provided by the guest atoms in a clathrate compound can be compensated by the Al atoms in the framework. Approaching the Zintl composition, a monotonic decrease of the carrier concentration with increasing Al content is expected. At the Zintl composition, the charge carriers inserted by the guest atom should be ideally completely absorbed by the 16 Al substituents in the framework, and the DOS at the Fermi level should become zero (semiconductor). Due to this proposed feature, the DOS is an important quantity to look at.

In Fig. 7.1, the DOS at the Fermi level is depicted for both clathrate compounds. On the left side, the $\text{DOS}(E_F)$'s of the configurations corresponding to the training set (for which *ab-initio* calculations are available) are shown for $\text{Ba}_8\text{Al}_x\text{Si}_{46-x}$, on the right side the same is shown for $\text{Sr}_8\text{Al}_x\text{Si}_{46-x}$. The colors of the dots are the same as in the GSS plots for each iteration. The black dashed line connects the $\text{DOS}(E_F)$'s of the GSSs. For $\text{Ba}_8\text{Al}_x\text{Si}_{46-x}$, the $\text{DOS}(E_F)$ of the GS structures decreases with the number of Al atoms. From $x = 13$ onwards, it increases slightly and decreases again until it reaches zero at $x = 16$. This means that at the Zintl composition, we find semiconducting behavior. In general, this trend is also present for non-GS structures. Furthermore, the $\text{DOS}(E_F)$ shows the same behavior for GSSs with LDA and PBEsol. Similarly, for the Sr clathrates it reveals a slight increase in the region of high x , reaches a maximum, and then approaches zero at $x = 16$. The kink in the region $x=12-13$, for both compounds indicates a change of the electronic behavior by approaching the Zintl composition. Due to this feature, the separation of the composition range around $x = 13$ and performing two CEs for low and high x , respectively, is justified. In the region of low x , there is no monotonic decrease of the $\text{DOS}(E_F)$ as compared to the Ba clathrate. This results from a different behavior of the band structures for Sr as seen below (Fig. 7.3). In contrast to $\text{Ba}_8\text{Al}_6\text{Si}_{40}$, where the $\text{DOS}(E_F)$ reaches a local maximum, for $\text{Sr}_8\text{Al}_6\text{Si}_{40}$ it has a local minimum.

Since the $\text{DOS}(E_F)$ approaches zero at the Zintl composition, the electronic behavior of these structures is studied in more detail. Figure 7.2 illustrates the DOS around the Fermi level for $\text{Ba}_8\text{Al}_{16}\text{Si}_{30}$ (left) and $\text{Sr}_8\text{Al}_{16}\text{Si}_{30}$ (right) for different configurations taken from the GSSs (obtained with PBEsol). Their energies and

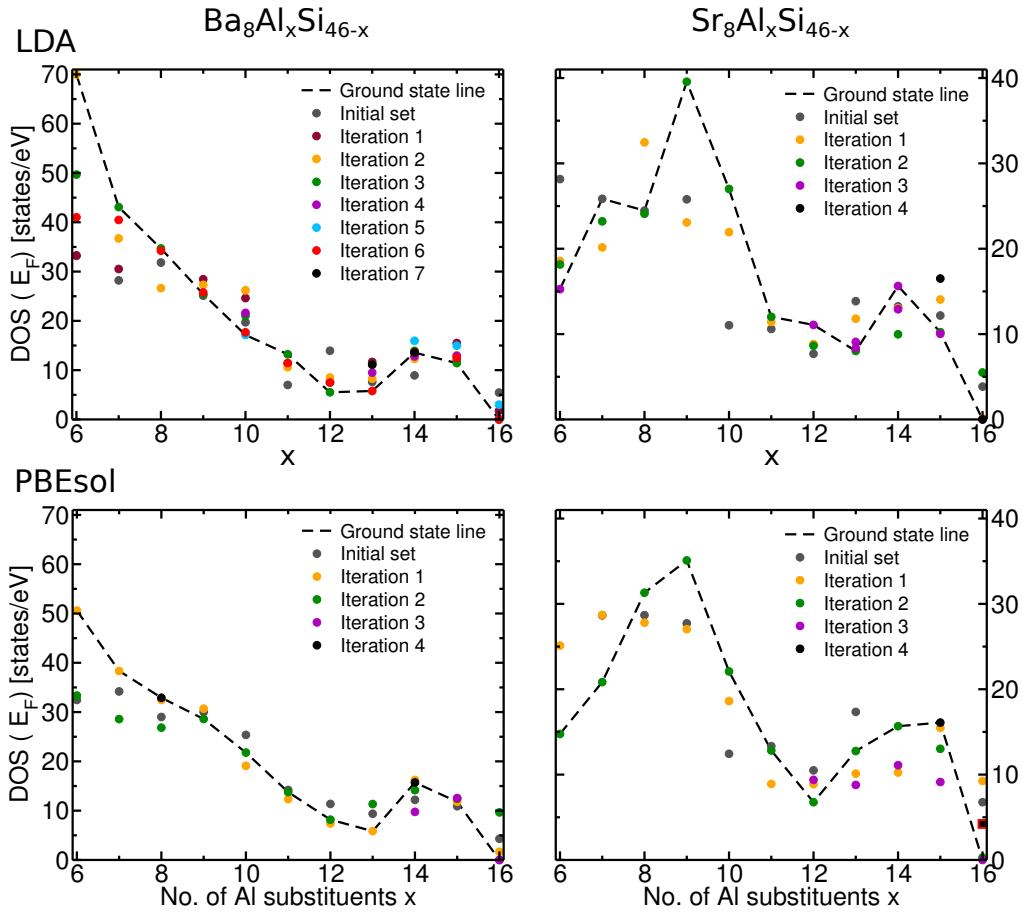


Figure 7.1: Density of states at the Fermi level $\text{DOS}(E_F)$ for $\text{Ba}_8\text{Al}_x\text{Si}_{46-x}$ (left) and $\text{Sr}_8\text{Al}_x\text{Si}_{46-x}$ (right) as obtained from LDA (upper panels) and PBEsol (lower panels).

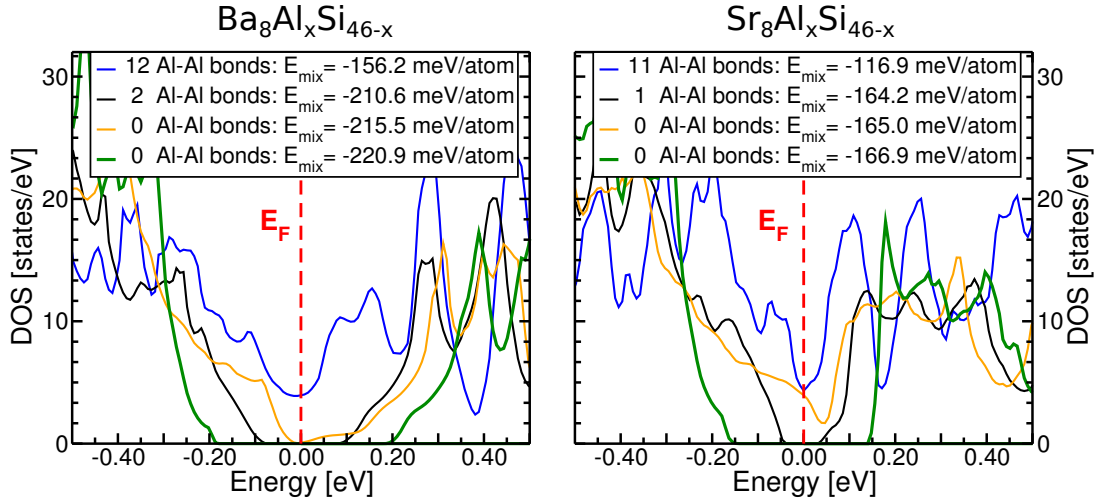


Figure 7.2: Density of states (DOS) for structures of the Zintl composition calculated with the PBEsol functional for the Ba (left) and the Sr clathrate (right).

electronic behavior are summarized in Tab. (7.1). (Results from the GSSs with LDA are similar. They can be found in the Appendix, Sec. B.1.) The configurations with a large number of Al-Al bonds clearly reveal metallic behavior. Furthermore, there exist structures with a few Al-Al bonds and a small Kohn-Sham band gap

E_g . The structures with no Al-Al bonds are lower in energy, but not all of them show semiconducting behavior. However, for both clathrate compounds the GS configuration has the largest band gap with respect to other configurations. The band gap of the GS is smaller for the Ba clathrate ($E_g = 0.36$ eV) than for the Sr clathrate ($E_g = 0.30$ eV). For the empty non-substituted clathrate Si_{46} , a larger band gap of $E_g = 1.3$ eV from LDA calculations [49] is reported. Thus, the guest atoms and the Al doping lead to a decrease of the band gap.

	Configuration ($24k, 16i, 6c$) N_b	e_{mix} [meV/atom]	M/SC	E_g [eV]
Ba	(9,5,2) 12	-156.2	M	-
	(8,4,4) 2	-210.6	SC	0.16
	(6,6,4) 0	-215.5	M	-
	(12,1,3) 0	-220.9	SC	0.36
Sr	(9,5,2) 11	-116.9	M	-
	(8,4,4) 1	-164.2	SC	0.08
	(6,6,4) 0	-165.0	M	-
	(12,1,3) 0	-166.9	SC	0.30

Table 7.1: Structures of the Zintl composition with metallic (M) and semiconducting (SC) behavior.

In Ref. [24], a metallic behavior of the Zintl composition $\text{Sr}_8\text{Al}_{16}\text{Si}_{30}$ was reported from quantum chemical calculations. In that work, they studied the configuration with the 16 Al atoms located at the $16i$ sites of the host structure. This structure has 8 Al-Al bonds, since each i -site is linked to another i -site. The Al-Al bonds lead to a closing of the band gap, similar to what was observed for the configuration with 11 Al-Al bonds from Fig. 7.2 and Tab. (7.1). This emphasizes the fact that the electronic structure highly depends on the configuration of the clathrate compound. The semiconducting behavior of some Zintl configurations, including the GS, is thus an important finding of this thesis, which highlights them as promising candidates for thermoelectric applications.

The band structures together with the DOS are illustrated for both clathrates with the number of Al atoms $x = 6$ and $x = 16$ in Fig. 7.3. In the latter case, they reveal an indirect band gap with valence band maximum at the Γ point and the conduction band maximum at the M-point. In the case of $x = 6$, a gap appears well below the Fermi level at around -1.2 eV for Ba and around -1.05 eV for Sr. This and the fact that the band gap of the Sr clathrate of $E_g = 0.25$ eV is smaller than for Ba ($E_g = 0.45$ eV at $x = 6$) agrees well with the results of [24]. At the Zintl compositions, the gap, previously found below E_F , is now centered at the Fermi level and its size is a bit larger in the case of Sr, slightly reduced in the case of Ba. This differs from the result of the closing of the small band gaps at $x = 6$ by increasing the Al content as suggested in [24]. The reason for this discrepancy is explained by the fact that the configurations in [24] were not the GS's (see discussion above).

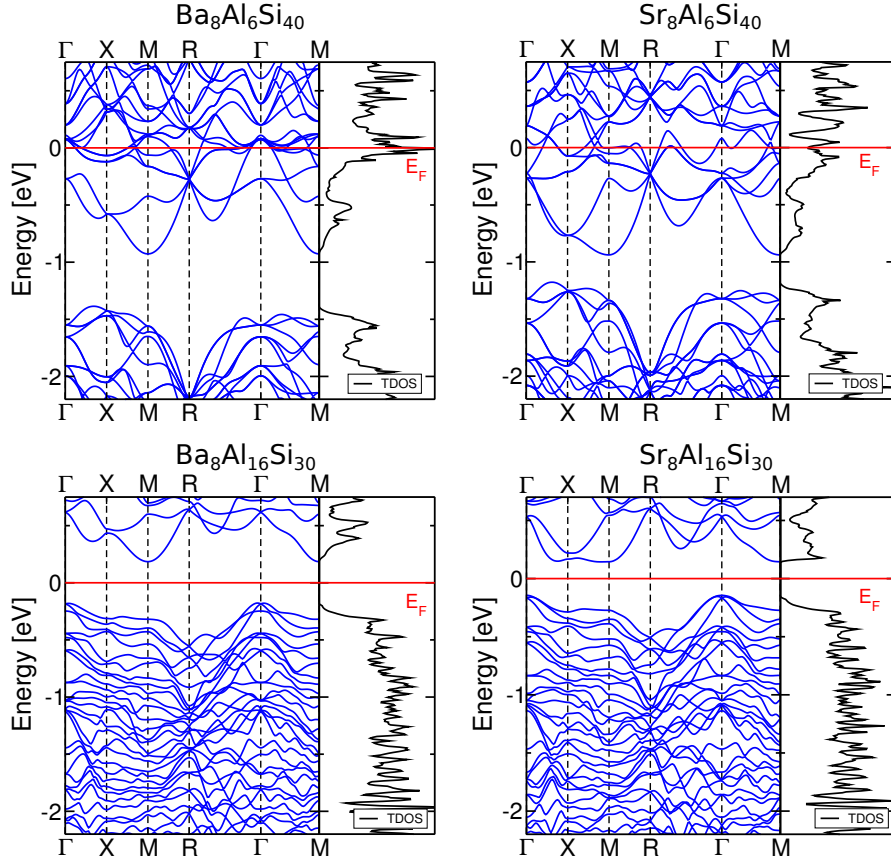


Figure 7.3: Band structure and density of states for $X_8Al_6Si_{40}$ (top) and $X_8Al_{16}Si_{30}$ (bottom) from calculations with PBEsol. left: $X=Ba$ and right: $X=Sr$.

7.2 Structural properties

7.2.1 Lattice constants

The lattice constant a of the GS structures with respect to the number of Al substituents is presented in Fig. 7.4, for the Ba (dots) and the Sr (triangles) clathrates. Both compounds reveal a linear increase of a confirmed by both functionals, LDA (blue lines) and PBEsol (red lines), respectively. The rate $\Delta a/\Delta x = m \approx 0.018 \text{ \AA}$ for Ba (see Tab. (7.2)) is close to the experimental value of 0.02 \AA [24, 50]. The lattice constant for Sr changes similarly with $m \approx 0.020 \text{ \AA}$. The monotonic increase of a with respect to the Al content for both compounds is explained by the fact that the radius of Al atoms is larger than that of Si atoms [51]. The smaller size of the Sr atoms in comparison to the Ba atoms [51] leads to a lattice parameter of the Sr-filled clathrate that is around 0.07 \AA smaller than that of the Ba-filled clathrate. This almost constant shift is present in the entire composition range.

$a(x) = a_0 + mx$	Ba (LDA)	Ba (PBEsol)	Sr (LDA)	Sr (PBEsol)
a_0 [\AA]	10.2289	10.2937	10.1421	10.2110
m [\AA]	0.0179	0.0186	0.0200	0.0207

Table 7.2: Linear fit of the lattice constant vs. the number of Al substituents x .

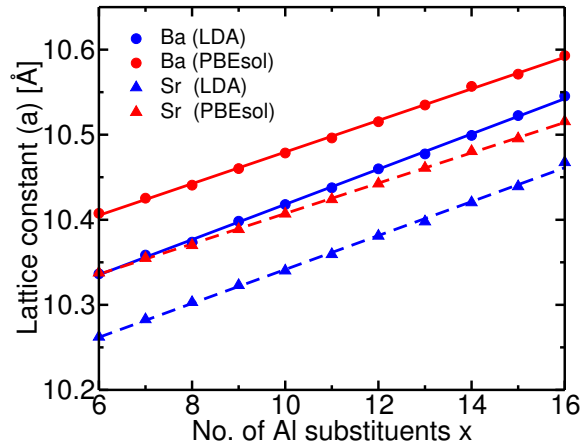


Figure 7.4: Lattice constant vs. the number of Al substituents for the GS structures.

As expected, the lattice parameters obtained by the LDA functional are around 0.065 \AA smaller than the results of PBEsol. It is known from Ref. [52] that for alkaline-earth metals, as Sr and Ba, LDA underestimates a by more than 2% (relative error), whereas a value closer to experiment is found with PBEsol. Furthermore, the lattice constant for simple solids Al (face-centered-cubic structure) and Si (diamond structure) compares well (relative error less than 0.5%) for both functionals. For the clathrates the results from PBEsol calculations compare well with the experimental values, as seen in Tab. (7.3). The PBEsol functional still underestimates the value of a , but the relative error is around or below 0.5% for the entire composition range in case of the Ba clathrate. For the Sr clathrate, only one composition at $x = 10$ could be synthesized [24]. Its calculated lattice constant is also within an accuracy of 0.5%.

		Lattice constant a [Å]					
		x=7	x=8	x=10	x=12	x=14	x=15
Ba	PBEsol	10.425	10.441	10.479	10.515	10.557	10.571
	Exp. [24]			10.515		10.620	
	Exp. [25]		10.493	10.533	10.572		10.636
	Exp. [50]		10.486	10.525	10.563	10.602	10.621
	Exp. [53]	10.465					
	Δa_{\max}	0.04	0.052	0.054	0.057	0.063	0.065
Sr	PBEsol			10.4179			
	Exp. [24]			10.4495			
	Δa_{\max}			0.0316			

Table 7.3: Comparison of calculated lattice constants with experiments. Δa refers to the maximum difference between experiment and calculation.

7.2.2 Bond distances

In Fig. 7.5, the average bond distances for the GS configurations reveal a dependence on the number of Al substituents (dashed lines - LDA, solid lines - PBEsol).

Focusing on the Ba clathrate (Fig. 7.5 (left)), the $i-i$ and $k-i$ bonds show a monotonic (almost linear) increase with the Al content in the low x range. Taking

into account the GS configurations (see Tab. (6.5)), at $x = 6$ all Al atoms are placed at the $6c$ position. With an increase of the Al content, the additional Al atoms of the GS structures begin to occupy the i sites. This is caused by the avoidance of Al-Al bonds, which are energetically unfavorable. This results in a larger distance of bonds containing an i site, i.e., the $i-i$ and $i-k$ bonds. The larger bonds when an Al atom is involved can be explained by the larger size of Al in comparison to Si [51]. This is related to the linear increase of the lattice constant (explained above). Since no k site is occupied in the range of low x , the $k-k$ bond distance remains almost constant or decreases slightly. As shown in Sec. 6.2 (Tab. (6.5)), an occupation of the k site appears from $x = 13$ onwards what leads to a drastic increase of the $k-k$ bond and a decrease of the $i-i$ bond from $x = 12$ to $x = 13$. This trend continues until the Zintl composition is reached, where the k site is half occupied for the GS configuration. The bond $k-c$ is almost independent of the Al content. This becomes clear by looking at the Al occupations of the c and k sites. At low x , the full occupation of the c sites and no k occupation imply that one Al atom is part of the $k-c$ bond. At high x , the c position is less occupied. A c site without an Al atom allows for an occupation of the Al at the nearest-neighbor k sites, since no Al-Al bond can result from them. Thus, an unoccupied c site (Si) is surrounded by occupied k sites, and still one Al atom is involved in the $k-c$ bond. The length of the $k-c$ bond is not affected by the allocation of the Al atom at the c or k site.

The trends of the low substitutional range for the Sr clathrate are similar to the Ba case (Fig. 7.5 (right)). However, the increase of the bond distances for the $i-i$ and $i-k$ continues further until the composition of $x = 15$. This is again related to the preferred occupation of the i site for GS structures. At $x = 16$, the ordering of the configurations changes abruptly, and the bond distances again look similar to those of the Ba clathrates.

In general, the bond distances from calculations with the LDA functional are about 0.02 \AA smaller than from PBEsol. Note that for each x , the GSSs with the two functionals lead to the same GS configurations. Consequently, the differences in bond lengths are basically always the same. For the Ba clathrate, the experimental bond distances and the values calculated values with PBEsol compare well for the compositions $x = 7$, $x = 10$ and $x = 15$, as shown in Tab. (7.4). Here, the differences are typically below 0.01 \AA , and only in some cases larger than 0.02 \AA (bold values).

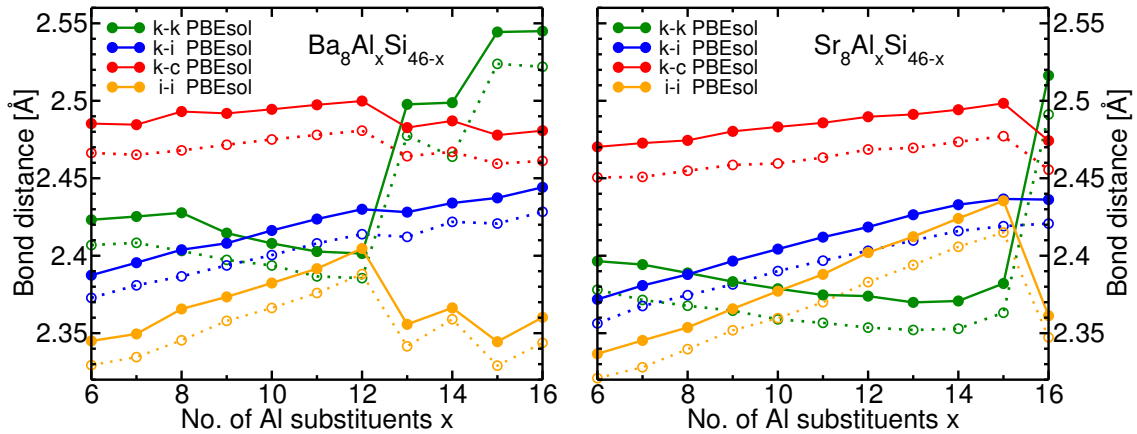


Figure 7.5: Average bond distances of the ground states for the Ba (left) and Sr (right) clathrates from PBEsol (solid lines) and LDA (dashed lines).

Bond distances d in [\AA] for the Ba clathrates								
	x	7	6.9	10	10	10	15	15
	Sites	PBEsol	Exp. [53]	PBEsol	Exp. [24]	Exp. [25]	PBEsol	Exp. [25]
Ba	$i-i$	2.350	2.356(3)	2.3824	2.3771(2)	2.386(3)	2.3445	2.483(7)
	$k-i$	2.396	2.401(1)	2.4163	2.4204	2.4244(8)	2.4373	2.436(2)
	$k-k$	2.425	2.447(4)	2.4080	2.397(2)	2.441(2)	2.5444	2.553(4)
	$k-c$	2.485	2.494(2)	2.4945	2.4996	2.504(1)	2.4779	2.485(2)
Sr	$i-i$			2.3771	2.3786(2)			
	$k-i$			2.4043	2.4110			
	$k-k$			2.3787	2.3933(2)			
	$k-c$			2.4831	2.4871			

Table 7.4: Comparison of the bond distances calculated with the functional PBEsol with experiments.

Analogously to Fig. 7.5, in Fig. 7.6 we show experimental data as extracted from Refs. [53] and [25] for the Ba case. The experimental bond distances $k-c$ and $k-i$ are in very good agreement for the entire composition range. The experimental $k-k$ distance is slightly larger for low x , what suggests a presence of Al at the k site in the measured material composition (find a detailed discussion of k occupation at low x in the next section). Another plausible reason is that the $k-k$ bond lies parallel to the $[100]$ direction, thus the theoretical underestimation of a will mainly affect the $k-k$ bond. For high x , again a good correspondence between calculation and experiment is achieved for the $k-k$ bond. In case of the $i-i$ bond distance, its slight increase at low x is also captured by theory, whereas large differences are revealed at high x . The $i-i$ bond length is much larger in experiment than in the calculations. The discrepancy at high x can be explained by taking into account the annealing temperature of $T = 900^\circ\text{C}$ in Refs. [53] and [25]. A temperature of 900°C corresponds to an energy $k_B T \approx 100$ meV which is above to the energy cost of 85 meV paid by moving an Al atom from the k to the i site (energy value taken from Tab. (6.4)). An increase of the Al occupation at the i site leads to an increase of the $i-i$ bond.

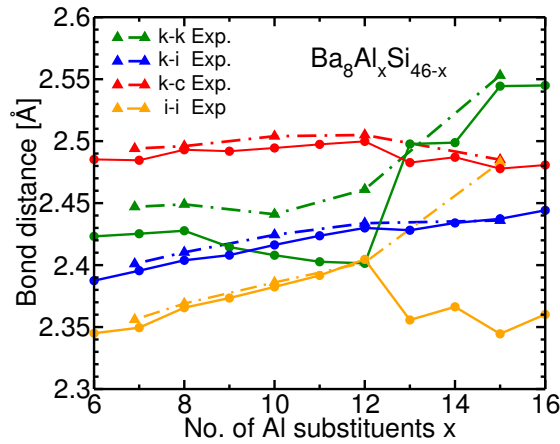


Figure 7.6: Bond distances of the Ba clathrate from experiments [53, 25] (triangles connected with dash-dotted lines) are shown together with the calculated ones (functional PBEsol, dots connected with solid lines).

Referring to another experiment [50], the sample was annealed at a similar temperature, *i.e.*, 1000-1300 K. In addition, the temperature at which the measurement was performed was reported as 35 K. Here, the trends for bond distances agree even better with the calculations. In line with our calculations, a decrease of the *i-i* bond at high *x* could be revealed by this measurement, and also the *k-k* bond distance at low *x* is closer to the calculations.

To conclude, the occupation of the Wyckoff positions strongly affects the bond distances. They can be directly measured, whereas the occupation of the sites with either Al or Si atoms cannot be clearly distinguished by X-ray diffraction [17, 24, 50, 53]. Hence, one way to estimate the occupancies is through the use of models relating the bond distances to the site occupancies. With the CE of the energy, as we have performed for the GSS, the site occupancies at finite temperature can be obtained directly (discussed in the following section). To study the changes of the bond distances with temperature, a CE for bond distances could be performed. This and the model relating the bond distances to the site occupancies will form part of future work.

7.2.3 Occupancy factor

The CE allows for simulating the site occupancies at finite temperature, since the CE can predict the energy of any structure. In the discussion, it is always referred to the fractional Al site occupancies, usually named occupancy factor (OF), which represents the ratio between the number of Al atoms located at a certain site *v* and the total number of *v* sites. The OF is 1 if all of the *v* sites are occupied by Al atoms and 0 if no *v* site is occupied by Al.

To simulate the OFs at finite temperature *T*, an average of the OF for configurations at a fixed number of Al substituents is performed. The configurations are generated by a Metropolis walk through the configuration space. For each Metropolis step, the configuration is changed by swapping two randomly selected Al and Si atoms. An example of the Metropolis simulation is illustrated in Fig. 7.7 for temperature *T* = 1000 K and composition *x* = 10. First, an equilibration of the energy of the system is performed (left part in Fig. 7.7) with 10000 Metropolis steps. For *T* = 1000 K, the energy is already equilibrated after around 1500 steps, whereas at

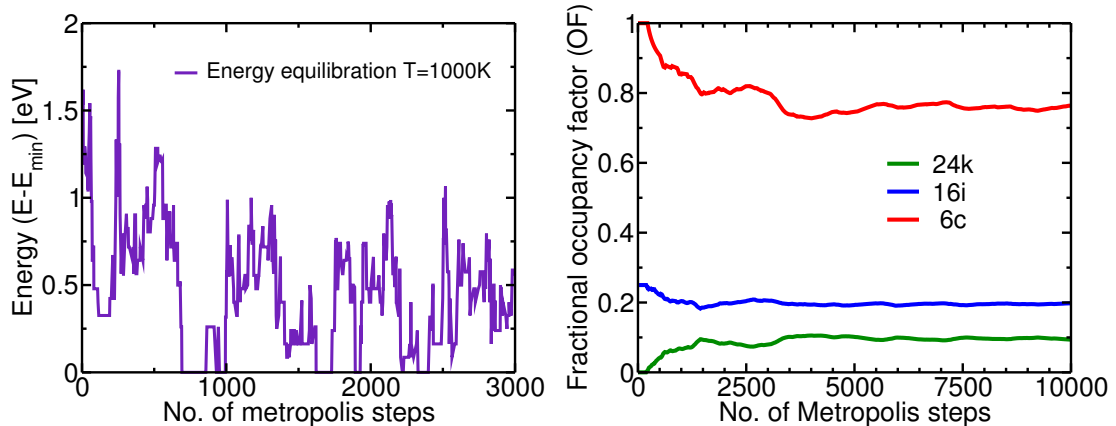


Figure 7.7: Example of the simulated occupancy factors for the three considered Wyckoff sites at *T* = 1000K (left) and the energy equilibration (right). Averaging of the occupancy factors has been performed at every 10th step.

low temperatures the energy equilibration requires more Metropolis steps. After the equilibration, the Metropolis sampling is performed for another 10000 steps and an average of the OFs every 10th step is taken. As it can be seen in the right part of Fig. 7.7, the OFs for 24*k*, for 16*i*, and 6*c* converge to a constant value after the 10000th Metropolis steps.

Before coming to the discussion of the OFs at finite temperature obtained from the two CE for the Ba and Sr clathrate, it has to be clarified why an overlap of the CEs at $x = 13$ is needed to achieve good results. In Fig. 7.8, the OFs for the Ba clathrate are simulated with the CE1 in the range $6 \leq x \leq 13$ and the CE2 in the range $14 \leq x \leq 16$ without an overlap. A drastic change of behavior appears between $x = 13 - 14$. In order to evaluate whether this change is physically motivated, an overlap of the CEs is introduced, and several splits are checked (discussion in Sec. 6.1). With an overlap in $x = 13$, the abrupt behavior is softened (Fig. 7.9 (left)). From the fact that the OFs for 24*k* and 16*i* still cross in this region, we conclude that our findings are indeed physical.

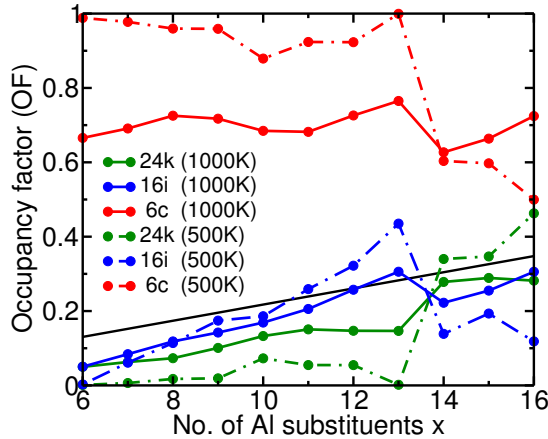


Figure 7.8: Fractional occupancy factor of the three Wyckoff positions from CEs without overlap, indicating a drastic change at $x = 13-14$.

The OF values for the *k* site (green), the *i* site (blue) and *c* site (red) of the Ba clathrate with respect to the number of Al substituents is illustrated in the left part of Fig. 7.9. Furthermore, the OF corresponding to the fully disordered structure (with identical OF for every site), $OF_{\text{dis}} = x/46$, where the occupation of the sites are considered as equally likely is indicated by the black solid line. At the temperature 1000 K, the OFs of the *k* and *i* site follow nearly the OF_{dis} . The OF of the *c* site is much larger and clearly indicates its preference. This preference has already been reported for different kinds of clathrate compounds [17]. At a lower temperature of 500 K, the *c* site is fully occupied in the low substitutional range ($OF(c)=1$). This site gets less occupied upon reaching the Zintl composition, similar to what has already been discussed for the GS configurations. The OFs of the *k* and *i* site at 500 K depart from each other as compared to the $T = 1000$ K case, and the *i* site is preferred over the *k* site for low x . At high x , a crossing of these OF appear at $x = 13$, and above $x = 13$ the *k* site is preferred over the *i* site. The change from a fully disordered configuration at high temperature and a distinct site preference at low temperature indicates an order-disorder transition upon heating. For the fixed composition of $x = 15$, the change of the OFs with respect the temperature is presented in Fig. 7.9 (right). Here, the departure of the $OF(k)$ from the $OF(i)$ occurs below a temperature around 800K.

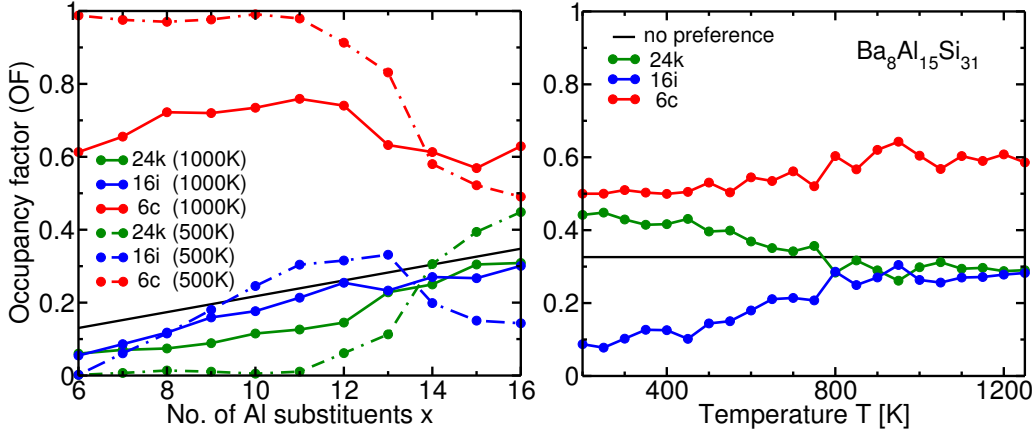


Figure 7.9: Fractional occupancy factor (OF) of the Wyckoff positions $24k$, $16i$, and $6c$ for $\text{Ba}_8\text{Al}_x\text{Si}_{46-x}$ (left) as a function of the Al substituents x and OF as a function of temperature at $x = 15$ (right).

With a simulation of the OFs for the entire composition range and for various temperatures, the dependencies of the order-disorder transition can be further analyzed. In the left part of Fig. 7.10, the differences of the OF are illustrated for the k and i sites for the Ba clathrate. The violet color indicates an OF larger for the i site than for the k site, whereas green refers to a preference of the k site. The transition from a disordered state with similar OF of i or k site to an ordered state where the site i is preferred over k appears around 600 K to 900 K for low x up to 12. At $x = 13$, such a transition is not present for the entire temperature range. For high x , the transition to a k preference occurs around 800 K, more clearly seen from the plot in the right part of Fig. 7.9.

Such an order-disorder transition can be studied in an accurate way by applying statistical methods. A useful method to have access to the statistical quantities is the Wang-Landau algorithm [54]. With this method, the configurational density-of-states (CDOS) of the system can be calculated. Afterwards, all other quantities, e.g. the canonical distribution, can be derived from the CDOS. From the canonical distribution, the transition temperature can be determined, and the order of the phase transition classified. Here, the order parameter for the phase transition would be the difference of the two OFs for the k and i site. A first approach into this topic

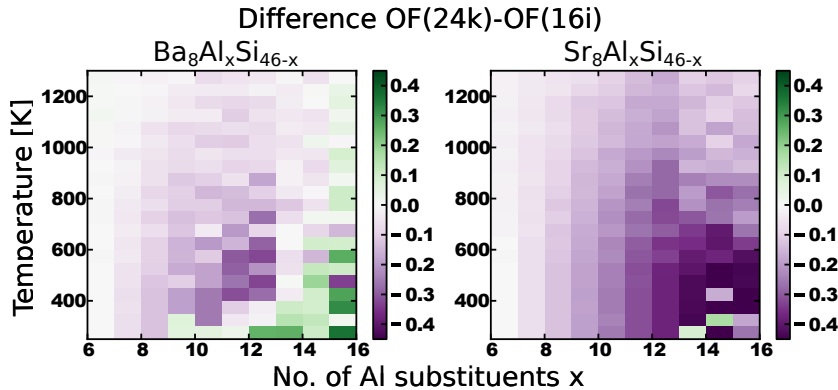


Figure 7.10: Differences of the fractional occupancy factor of the $24k$ and $16i$ sites: $\text{Ba}_8\text{Al}_x\text{Si}_{46-x}$ (left) and $\text{Sr}_8\text{Al}_x\text{Si}_{46-x}$ (right).

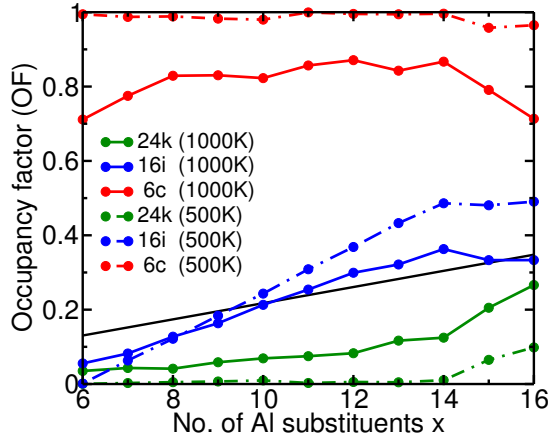


Figure 7.11: Fractional occupancy factor (OF) of the Wyckoff positions $24k$, $16i$, and $6c$ for the Sr clathrate as a function of the number of Al substituents x .

is discussed in the appendix, Sec. B.2.

Returning to the analysis of the OFs for the Ba clathrate, the configuration at finite temperature for the composition of $x = 7$ can be compared directly with experimental results of a similar composition ($x = 6.9$) [53]. In the experiment, a full occupation of the c site was reported which is in good agreement with the calculated GS configuration as well as with the finite temperature simulations. Furthermore, an occupation of the k site is revealed [53]. This conflicts with the preference for the i site obtained by the OFs simulations at a low finite temperature as well as for the GS configuration. A reason for this disagreement can be the annealing temperature of 900 K used in [53]. As seen from the discussion above, the transition temperature for low x is expected to be around 900 K or below. Thus, above or at 900 K, the clathrate configuration still shows the behavior of the disordered phase and thus, an occupation of the k site instead of the i site is equally likely.

After the detailed discussion of the Ba clathrate, we will focus on the OFs for the Sr clathrate (see Fig. 7.11). Similar to the Ba clathrate, the c site has a strong preference. Also, the OFs for site k and i at high temperature (1000 K) are close to the OF_{dis} . However, already at this temperature, the OFs of the k and i sites reveal a splitting in the intermediate region. This splitting is even increased at low temperatures (500 K). The trend of occupying the i sites terminates around $x = 14$, and the $\text{OF}(i)$ saturates in the region of high x . We suppose that the saturation results from reaching half occupation of site i at $x = 14$ (6 atoms at the c position and 8 atoms at the i position gives in total 14 Al atoms). An additional Al atom at the i site would lead to an unfavorable Al-Al bond, since the i site binds to another i site. However, the GS configuration at the Zintl composition indicated by half occupation of the c and k sites is still not yielded at $T = 500$ K. Thus, a configuration similar to the GS is expected to occur at a lower temperature. So, in order to explore low temperatures close to the GS, other schemes to simulate the finite-temperature dependence could be applied. For instance, a possibility is the simulated annealing [55] with a reduction of the temperature during the Metropolis walk. In general, the OFs of the Sr clathrate do not reveal a change of preferences with increasing Al content. This is made clear with the temperature and composition-dependent plot of the OF differences for k and i sites (see Fig. 7.10 (right)).

As an overview, the fractional OFs dependent on the composition x and on

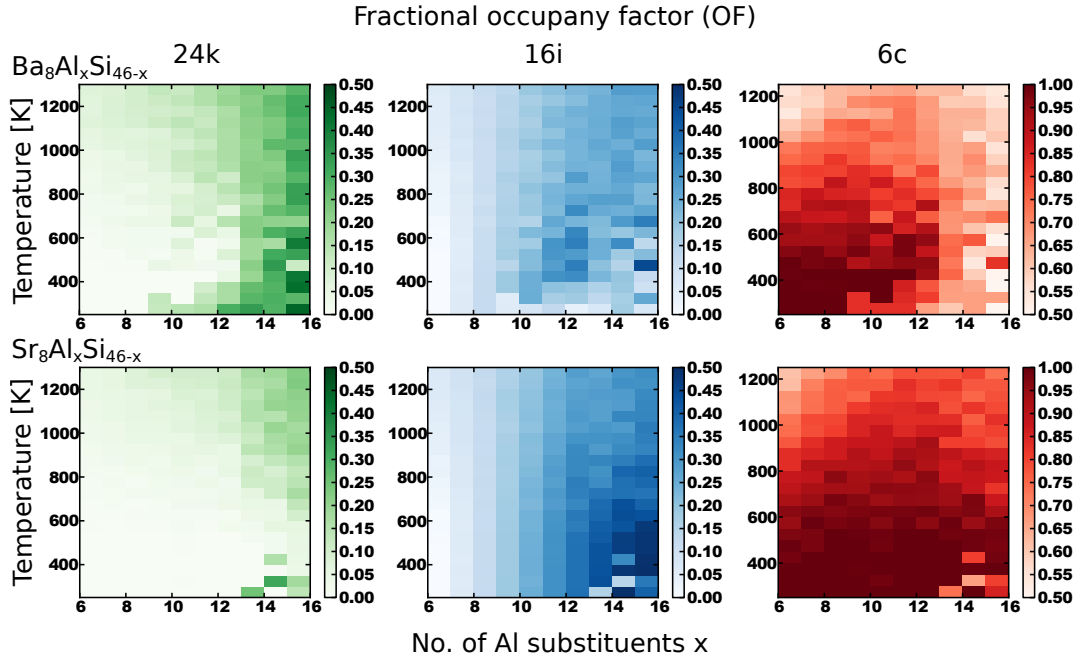


Figure 7.12: Fractional occupancy factor for $\text{Ba}_8\text{Al}_x\text{Si}_{46-x}$ and $\text{Sr}_8\text{Al}_x\text{Si}_{46-x}$ as a function of composition x and temperature T . The respective color code is given at the right side of each panel.

the temperature are presented for both clathrates in Fig. 7.12. The color code for the Wyckoff sites is like before (green k , blue i , red c). Intense color regions indicate a high occupation of the site, whereas white regions represent no occupation in case of $\text{OF}(k)$ and $\text{OF}(i)$ and half occupation in case of $\text{OF}(c)$. The OFs for Ba compounds are shown in the upper part, and the OFs for Sr compounds in the lower part. Although the structure of the clathrates is the same, they behave differently in the high-substitutional range. In case of $\text{Ba}_8\text{Al}_x\text{Si}_{46-x}$, there is a change of preference with increasing Al content. Furthermore, two different kinds of order-disorder transitions are revealed (i preference for low x and k preference for high x). The order-disorder transition is also present for $\text{Sr}_8\text{Al}_x\text{Si}_{46-x}$, whereas only a preference for the i site could be seen from the simulations. For Sr as guest, a configuration desired for technology (semiconductor) is more difficult to reach, since the favorable structure ordering at the Zintl composition is abruptly reached with respect to composition and temperature.

As it can be seen from the 2d plots of the OFs at low temperatures, the color of some rectangles fall out from their neighborhood. This is due to a trapping of the system at a local minimum if the simulation temperature is too low for crossing energy barriers. As improvements for studying the OFs, different finite-temperature simulation methods can be applied as the simulated annealing [55] (already mentioned above). Furthermore, a scheme using many walkers through the configurational space at different temperatures and exchanging them once in a while (the so-called “replica exchange” method) could also help to reach the real OF value without getting trapped in a local minimum.

Additionally, clearly visible from the 2d plots, the coarse grained composition range leads to poor resolution. Thus, only integer values of the site occupancy can be obtained with the unit cell. To yield a better resolution, one would need to make use of supercells. Supercells give access to fractional compositions, as, for instance,

$x = 6.9$ which is desirable due to the experiment in Ref. [53].

8 Conclusions and outlook

In the present work, we have investigated the clathrate compounds $\text{Ba}_8\text{Al}_x\text{Si}_{46-x}$ and $\text{Sr}_8\text{Al}_x\text{Si}_{46-x}$ ($6 \leq x \leq 16$) with respect to their structural stability and electronic properties. Their large configurational space is studied with a special iterative CE technique for large parent cells (code **CELL**). Applying the CE technique, the search of the GS configurations at each composition is performed for both clathrate compounds, by *ab-initio* calculations using the two exchange-correlation energy functionals, LDA and PBEsol. Due to a change of the electronic properties around the composition $x = 13$, the composition range is separated into two regions with an overlap at $x = 13$. With a set of 20-40 *ab-initio* calculations in each region, a CE with a predictive power of about 1-2 meV/atom is obtained (except for the GSS of $\text{Sr}_8\text{Al}_x\text{Si}_{46-x}$ with PBEsol where less random structures are included in the CE construction). The CE usually consists, apart from the empty cluster, of three 1-point clusters and four 2-point clusters representing the nearest-neighbor interactions. The error of the CE predictions is close to the accuracy of *ab-initio* calculations and no further improvement was found by adding new clusters to the CE. The GS configurations obtained by independent GSS's are the same for both energy functionals, emphasizing the applicability of the CE approach and the reproducibility of the results.

Regarding the GS configurations, the energetically unfavorable Al-Al bonds are avoided. Regarding the three Wyckoff positions $24k$, $16i$, and $6c$ of the host structure, there is a clear preference for Al atoms to occupy the c site. In case of Ba, a transition from a full c occupation to half c occupation takes place from the composition $x = 12$ to $x = 16$ (Zintl composition). The GS configurations of the Sr clathrate reveal a constant increase in the occupation of the i site up to $x = 15$ and a drastic configurational reordering at $x = 16$. Both clathrate types have the same GS configuration at the Zintl composition with 12 atoms at the k site (half occupancy), one atom at the i site and 3 atoms at the c site (half occupancy), thereby completely avoiding Al-Al bonds. The identification of such a configuration as the GS is one of the main results of this thesis, as it reveals semiconducting behavior with a Kohn-Sham band gap of $E_g = 0.36$ eV for Ba and $E_g = 0.60$ eV for Sr (PBEsol calculation), giving a perspective towards its technological relevance. The structural ordering leads to a metal-semiconductor transition at the Zintl composition, and furthermore, strongly influences the electronic properties at other compositions.

We found a linear increase of the lattice constant with the number of Al substituents (0.018 Å per addition in case of Ba and 0.02 Å in case of Sr) confirming experiment (0.02 Å for Ba). Furthermore, the distances of the k - c and the k - i bonds agree very well with the experiment for the entire composition range. The only discrepancies are observed for the k - k bond distance at low x and the i - k bond distance

at high x . However, they can be explained by the combination of two effects: (i) a finite temperature effect allowing for an Al transfer between k and i sites, and (ii) the sensitivity of the k - k bond distance to the lattice constant, which is slightly underestimated by the *ab-initio* calculations. In this respect, we found a strong correlation between the bond distances and the Al occupancy of the Wyckoff sites which cannot be directly obtained by measurements as X-ray diffraction. With the investigation of the Al occupancy factors at finite temperature, the substitutional configurations present an order-disorder transition around 600-900 K.

The findings of this thesis leave room for further work. Considering improvements in the CE construction, instead of the minimization of the mean-squared error other techniques with less tendency of overfitting should be used. A possible alternative is the CS technique, selecting the most relevant clusters for the CE from a large pool of clusters. The methods to realize the CS technique are not limited to the rather simple LASSO approach (example shown in appendix, Sec. B.3), but more complex alternatives such as the split Bregman iteration can be applied. Complex schemes may allow for using an initial guess of the ECIs as an additional input parameter. An alternative fitting method to obtain the ECIs could sense additional clusters to improve the predictability of the CE.

Furthermore, the technological relevant Zintl composition with its configurational dependent metal-semiconducting transition could be explored in detail using hybrid exchange-correlation functionals of DFT which usually yield values of band gaps closer to experiment.

Looking at the structural properties, the strong dependence of the bond distances on the Al occupancy factors suggests to develop models from it. For this purpose, we can perform a CE on the bond distance, in the same way as done on the energy. This would allow for access the temperature dependence of the bond distances, so as to help improving the models used by experimentalists. Besides this, the sampling methods available for finite-temperature simulations, as seen for the occupancy factor, can be extended to avoid local trapping. Schemes for this purpose would be simulated annealing, nested sampling, or other schemes with many walkers. The interesting finding of an order-disorder transition upon heating can be studied with the Wang-Landau algorithm. The implementation and preliminary results for the configurational density-of-states has already been performed, allowing us to extract some physical information (see appendix, Sec. B.2).

To yield better resolution in composition dependencies and to enhance the comparison between calculations and experiments, results for fractional compositions are desired. This would require the sampling of the configurational space in supercells, using the CEs already developed in this thesis.

Bibliography

- [1] M. G. Kanatzidis. Advances in thermoelectrics: From single phases to hierarchical nanostructures and back. *Material Research Society*, 40:687, 2015.
- [2] J. W. Bos. Thermoelectric materials: efficiencies found in nanocomposites. *Education in Chemistry*, pages 15–18, 2012.
- [3] A. Shakouri. Recent Developments in Semiconductor Thermoelectric Physics and Materials. *Annual Review of Material Research*, 41:399–431, 2011.
- [4] G. J. Snyder and E. S. Toberer. Complex thermoelectric materials. *Nature materials*, 7:105–114, 2008.
- [5] Renewable Energy Focus staff. Electricity from waste heat. Website, 2011. Online at: <http://www.renewableenergyfocus.com/view/15619/electricity-from-waste-heat>.
- [6] T. J. Seebeck. Über die magnetische Polarisation der Metalle und Erze durch Temperatur-Differenz. *Annalen der Physik*, 82:133–160, 1826.
- [7] F. J. DiSalvo. Thermoelectric Cooling and Power Generation. *Science*, 30:703–706, 1999.
- [8] A. J. Minnich, M. S. Dresselhaus, Z. F. Ren, and G. Chen. Bulk nanostructured thermoelectric materials: current research and future prospects. *Energy & Environmental Science*, 2:466–479, 2009.
- [9] G. Wiedemann and R. Franz. Über die Wärme-leistungsfähigkeit der Metalle. *Annalen der Physik*, 165:487–531, 1853.
- [10] G. A. Slack. *The Thermal Conductivity of Nonmetallic Crystals, Solid State Physics*, volume 34. Academic Press, New York, 1979.
- [11] D. M. Rowe. *CRC Handbook of Thermoelectrics*. CRC Press, 1995.
- [12] J. R. Sootsman, D. Y. Chung, and M. G. Kanatzidis. New and Old Concepts in Thermoelectric Materials. *Angewandte Chemie International Edition*, 48:8616–8639, 2009.
- [13] L.-D. Zhao, V. P. Dravid, and M. G. Kanatzidis. The panoscopic approach to high performance thermoelectrics. *Energy Environmental Science*, 7:251–268, 2014.

- [14] X. Shi, J. Yang, J. R. Salvador, M. Chi, J. Y. Cho, H. Wang, S. Bao, J. Yang, W. Zhang, and L. Chen. Multiple-filled Skutterudites: High Thermoelectric Figure of Merit through Separately Optimizing Electrical and Thermal Transports. *Journal of American Chemical Society*, 133:7837–7846, 2006.
- [15] H. Zhaoa, J. Sui, Z. Tang, Y. Lan, Q. Jie, D. Kraemer, K. McEnaney, A. Gulyoy, G. Chen, and Z. Ren. High thermoelectric performance of MgAgSb-based materials. *Nano Energy*, 7:97–103, 2014.
- [16] T. F. Fässler. *Zintl Phases*. Springer Verlag, 2011.
- [17] M. Christensen, S. Johnsen, and B. B. Iversen. Thermoelectric clathrates of type I. *Dalton Transactions*, 39:978–992, 2010.
- [18] S. Kim, S. Hu, C. Uher, T. Hogan, B. Huang, J. D. Corbett, and M. G. Kanatzidis. Structure and Thermoelectric Properties of $\text{Ba}_6\text{Ge}_{25-x}$, $\text{Ba}_6\text{Ge}_{23}\text{Sn}_2$, and $\text{Ba}_6\text{Ge}_{22}\text{In}_3$: Zintl Phases with a Ciral Clathrate Structure. *Journal of Solid State Chemistry*, 153:321–329, 2000.
- [19] N. P. Blake, D. Bryan, S. Lattturner, L. Mollnitz, G. D. Stucky, and H. Metiu. Structure and stability of the clathrates $\text{Ba}_8\text{Ga}_{16}\text{Ge}_{30}$, $\text{Sr}_8\text{Ga}_{16}\text{Ge}_{30}$, $\text{Ba}_8\text{Ga}_{16}\text{Si}_{30}$ and $\text{Ba}_8\text{In}_{16}\text{Sn}_{30}$. *Journal of Chemical Physics*, 114:10063, 2001.
- [20] E. S. Toberer, M. Christensen, B. B. Iversen, and G. Jeffrey Snyder. High temperature thermoelectric efficiency in $\text{Ba}_8\text{Ga}_{16}\text{Ge}_{30}$. *Physical Review B*, 77:075203, 2008.
- [21] A. Saramat, G. Svensson, A. E. C. Palmqvist, C. Stiewe, E. Mueller, D. Platzek, S. G. K. Williams, D. M. Rowe, J. D. Bryan, and G. D. Stucky. Large thermoelectric figure of merit at high temperature in Czochralski-grown clathrate $\text{Ba}_8\text{Ga}_{16}\text{Ge}_{30}$. *Journal of Applied Physics*, 99:023708, 2006.
- [22] B. C. Chakoumakos, B. C. Sales, R. Jin, D. G. Mandrus, and S. S. Nolas. Structural disorder and thermal conductivity of the semiconducting clathrates $\text{sr}_8\text{ga}_{16}\text{ge}_{30}$. *Journal of Alloys and Compounds*, 296:80–86, 2000.
- [23] B. C. Sales, B. C. Chakoumakos, R. Jin, J. R. Thompson, and D. G. Mandrus. Structural, magnetic, thermal, and transport properties of $\text{X}_8\text{Ga}_{16}\text{Ge}_{30}$ ($x=\text{eu},\text{sr},\text{ba}$) single crystals. *Physical Review B*, 63:245113, 2001.
- [24] J. H. Roudebush, N. Tsujii, A. Hurtando, H. Hope, Y. Grin, and S. M. Kazlarich. Phase range of the Type-I Clathrate $\text{Sr}_8\text{al}_{10}\text{si}_{36-x}$ and Crystal Structure of $\text{Sr}_8\text{Al}_{10}\text{Si}_{36}$. *Computational Material Science*, 59:101–107, 2012.
- [25] Michael Baitinger and Bodo Böhme. Private communications.
- [26] J. M. Sanchez, F. Ducastelle, and D. Gratias. Generalized cluster description of multicomponent systems. *Physica A*, 128:334–350, 1984.
- [27] G. D. Garbulksy and G. Ceder. Linear-programming method for obtaining effective cluster interactions in alloys from total-energy calculations: Application to the fcc pd-v system. *Physical Review B*, 51:67, 1995.

- [28] B. Hülsen, M. Scheffler, and P. Kratzer. Thermodynamics of the Heusler alloy $\text{Co}_{2-x}\text{Mn}_{1-x}\text{Si}$: A combined density functional theory and cluster expansion study. *Physical Review B*, 79:09447, 2009.
- [29] M. Stone. Cross-validation Choice and Assessment of Statistical Predictions. *Journal of the Royal Statistical Society B (Methodological)*, 36:111–147, 1974.
- [30] A. van de Walle and G. Ceder. Automating first-principles phase diagram calculations. *Journal of Phase Equilibria*, 23:348–359, 2002.
- [31] D. M. Allen. The relationship between variable selection and prediction. *Technometrics*, 16:125–127, 1974.
- [32] Knut Baumann. Cross-validation as the objective function for variable-selection techniques. *Trends in Analytical Chemistry*, 22:395–406, 2003.
- [33] L. J. Nelson, G. L. W. Hart, F. Zhou, and V. Ozoliņš. Compressive sensing as a paradigm for building physics models. *Physical Review B*, 87:035125, 2013.
- [34] R. Tibshirani. Regression Shrinkage and Selection via LASSO. *Journal of the Royal Statistical Society. Series B (Methodological)*, 58:267–288, 1996.
- [35] S. S. Chen, D. L. Donoho, and M. A. Saunders. Atomic Decomposition by Basis Pursuit. *SIAM Journal of Scientific Computing*, 20:33–61, 1998.
- [36] D. Lerch, O. Wieckhorst, G. L. W. Hart, R. W. Forcade, and S. Müller. UNCEL: a code for constructing cluster expansion for arbitrary lattices with minimal user-input. *Modelling and Simulation in Materials Science and Engineering*, 17:055003, 2009.
- [37] V. Blum, G. L. W. Hart, M. J. Walorski, and A. Zunger. Using genetic algorithm to map first-principles results to model Hamiltonians: Application to the generalized Ising model for alloys. *Physical Review B*, 72:165113, 2005.
- [38] G. L. W. Hart, V. Blum, M. J. Walorski, and A. Zunger. Evolutionary approach for determining first-principles hamiltonians. *Nature Materials*, 4:391–394, 2005.
- [39] G. L. W. Hart, L. J. Nelson, and R. W. Forcade. Generating derivative structures at a fixed concentration. *Computational Material Science*, 59:101–107, 2012.
- [40] S. Rigamonti, M. Troppenz, and C. Draxl, 2015. Cluster expansion for large parent cells (CELL).
- [41] A. Gulans, S. Kontur, C. Meisenbichler, D. Nabok, P. Pavone, S. Rigamonti, S. Sagmeister, U. Werner, and C. Draxl. exciting: a full-potential all-electron package implementing density-functional theory and many-body perturbation theory. *Journal of Physics: Condensed Matter*, 26:363202–26, 2014.
- [42] W. Kohn and L. J. Sham. Self-consistent equations including exchange and correlations effects. *Phys. Rev.*, 140:A1133, 1965.

- [43] D. M. Ceperley. Ground state of the fermion one-component plasma: A Monte Carlo study in two and three dimensions. *Physical Review B*, 18:3126–3138, 1978.
- [44] D. M. Ceperley and B. J. Alder. Ground State of the Electron Gas by a Stochastic Method. *Physical Review Letters*, 45:566–569, 1980.
- [45] J. R. Perdew and Y. Wang. Accurate and simple analytic representation of the electron-gas correlation energy. *Physical Review B*, 45:13244, 1992.
- [46] J. P. Perdew, A. Ruzsinszky, G. I. Csonka, O. A. Vydrov, G. E. Scuseria, L. A. Constantin, X. Zhon, and K. Burke. Restoring the Density-Gradient Expansion for Exchange in Solids and Surfaces. *Phys. Rev. Lett.*, 100:136406, 2008.
- [47] J. A. Nelder and R. Mead. A simplex method for function minimization. *Computer Journal*, 7:308–313, 1965.
- [48] F. D. Murnaghan. The Compressibility of Media under Extreme Pressures. *Proceedings of the National Academy of Science of the United States of America*, 30:244–247, 1944.
- [49] D. Connétable. First-principles calculations of carbon clathrates: Comparison to silicon and germanium clathrates. *Physical Review B*, 82:075209, 2010.
- [50] J. H. Roudebush, C. de la Cruz, B. C. Chakoumakos, and S. M. Kauzlarich. Neutron Diffraction Study of the Type I Clathrate $\text{Ba}_8\text{Al}_x\text{Si}_{46-x}$: Site Occupancies, Cage Volumes, and the interaction between the Guest and the Host Framework. *Inorganic Chemistry*, 51:1805–1812, 2012.
- [51] J. T. Waber and D. T. Cromer. Orbital Radii of Atoms and Ions. *The Journal of Chemical Physics*, 42:4116–4123, 1965.
- [52] P. Haas, F. Tran, and P. Blaha. Calculation of the lattice constant of solids with semilocal functionals. *Physical Review B*, 79:085104, 2009.
- [53] M. Bobnar, B. Böhme, M. Wedel, U. Burkhardt, A. Ormezi, Y. Prots, C. Drahten, Y. Liang, H. D. Nguyen, M. Baitinger, and Y. Grin. Distribution of Al atoms in the clathrate-I phase $\text{ba}_8\text{Al}_x\text{Si}_{46-x}$ at $x=6.9$. *Dalton Transactions*, 44:12680, 2015.
- [54] F. Wang and D. P. Landau. Efficient, Multiple-Range Walk Algorithm to Calculate the Density of States. *Physical Review Letters*, 86:2050–2053, 2000.
- [55] Igor Wegener. Simulated Annealing Beats Metropolis in Combinatorial Optimization. In L. Caires, G. F. Italiano, L. Monteiro, C. Palamidessi, and M. Yung, editors, *Automata, Languages and Programming*, volume 3580, pages 589–601. Springer Verlag, 2005.
- [56] M. Borg, C. Stampfl, A. Mikkelsen, J. Gustafson, E. Lundgren, M. Scheffler, and J. N. Andersen. Density of configurational states from First principles Calculations: The Phase Diagram of Al-Na Surface Alloy. *ChemPhysChem*, 6:1923–1928, 2006.

A Appendix

A.1 Additional convergence tests

Plots depicting convergence test of the lattice constant exemplarily for the Sr clathrate:

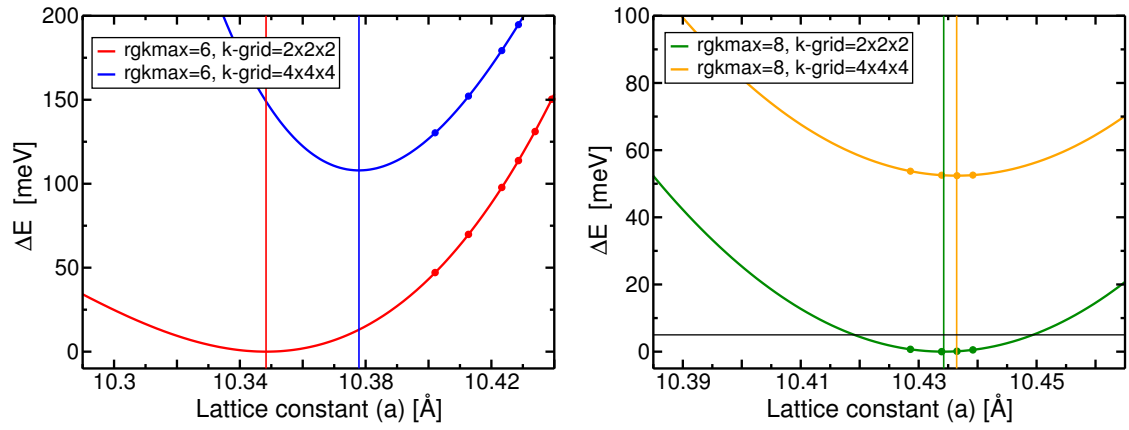


Figure A.1: Convergence test of the lattice constant for the Sr clathrate ($x = 6$, LDA). Fit of the energy versus the lattice constant a for $\text{rgkmax}=6$ (left) and $\text{rgkmax}=8$ (right). The minimum of the red (green) curve is chosen as zero in the left (right) panel. Energy difference between the minimum of the red and green curve is 1.93 meV.

A.2 Cluster expansion with the PBEsol functional

Plots depicting the final result of the GSSs with the PBEsol functional:

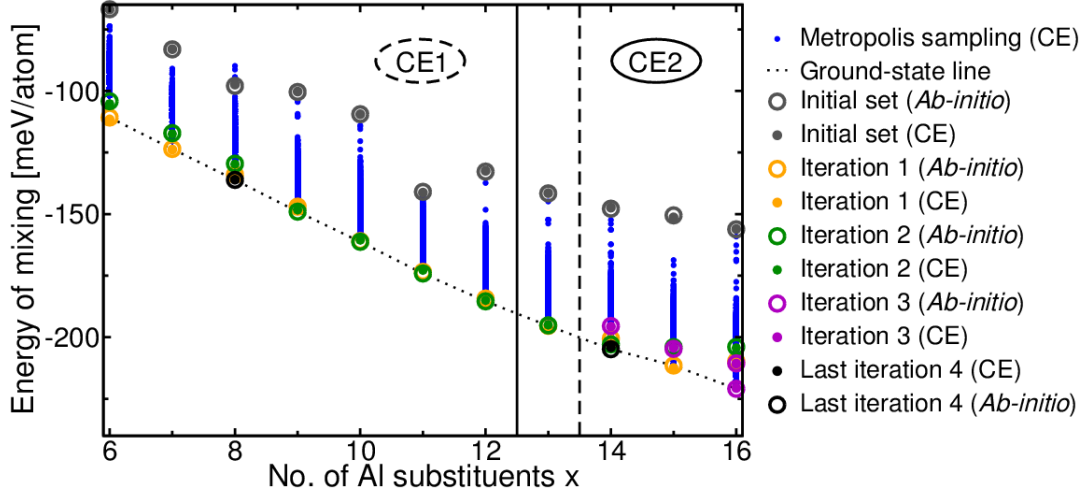


Figure A.2: Final result of the GSS for $\text{Ba}_8\text{Al}_x\text{Si}_{46-x}$ (PBEsol). Two CEs are performed: CE1 in the range $x \in [6, 13]$ and CE2 in the range $x \in [13, 16]$. CE1 and CE2 have an overlap at $x = 13$.

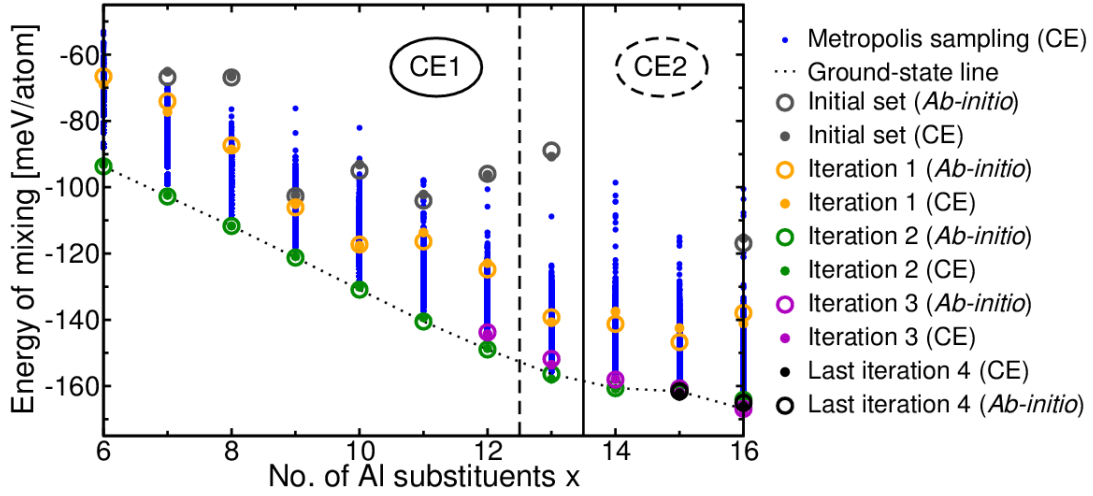


Figure A.3: Final result of the GSS for $\text{Sr}_8\text{Al}_x\text{Si}_{46-x}$ (PBEsol). Two CEs are performed: CE1 in the range $x \in [6, 13]$ and CE2 in the range $x \in [13, 16]$. CE1 and CE2 have an overlap at $x = 13$. Additionally, the random structure for $x = 12$ of the initial set is included in CE2 to improve the predictability.

B Appendix

B.1 Configurations of Zintl composition (LDA)

Energy of mixing and electronic properties for different configurations of the Zintl composition taken from the GSSs with LDA:

	Configuration ($24k, 16i, 6c$) N_b	e_{mix} [meV/atom]	M/SC	E_g [eV]
Ba	(9,5,2) 12	-155.5	M	-
	(2,8,6) 2	-209.4	M	-
	(8,4,4) 2	-216.8	M	-
	(12,1,3) 0	-224.1	SC	0.34
Sr	(9,5,2) 11	-107.1	M	-
	(3,8,5) 1	-154.4	M	-
	(6,6,4) 0	-157.3	M	-
	(12,1,3) 0	-159.8	SC	0.30

Table B.1: Structures of the Zintl composition with metallic (M) and semiconducting (SC) behavior.

B.2 First results using the Wang-Landau method

The Wang-Landau (WL) method [54] allows for calculating the CDOS of the system of interest. The temperature-independent CDOS enables the calculation of thermodynamic quantities, e.g. the temperature-dependent free energy $F(T)$ and internal energy $U(T)$. The WL method has been implemented as a tool in CELL.

The CDOS at an energy E is labeled as $g(E)$, where the total number of states is given by $\sum_E g(E)$. In order to test the WL implementation, the CDOS of the 2D Ising model is simulated. An example of the 4×4 Ising lattice is depicted in Fig. B.1, where the natural logarithm of $g(E)$ vs. the energy $e = E/N$ is shown. The black and the green line represented CDOS with different normalization schemes (formulas written in the legend). The CDOS is symmetrical around the y -axis ($e = 0$) as already reported for the 32×32 Ising lattice in Ref. [54] and references therein.

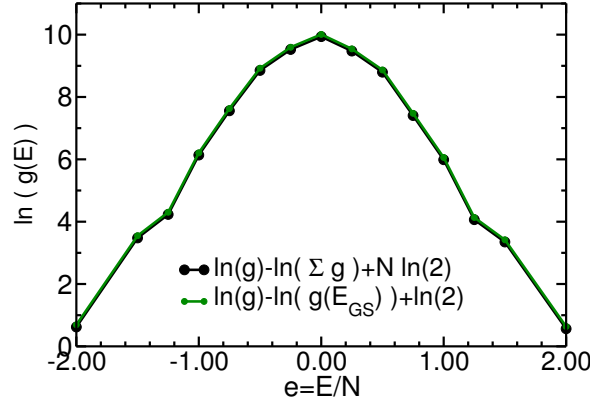


Figure B.1: Test of the WL method for the 4×4 Ising model. Here, the final modification factor is 1.0000001.

First tests to simulate the CDOS for the clathrates compounds have been performed. Figure B.2 (a) shows the natural logarithm of $g(E)$ vs. the energy of mixing e_{mix} . The black and green curves represent the CDOS with different normalizations (formulas in legend), for the black line the upper bound and for the green line the lower bound of the configurations at $x = 11$ (see Eq. (2.1) and Fig. 2.3 in Chapter 3) is used. With this CDOSs, $F(T) = k_B T \ln(Z)$ and $U(T) = \sum_E E g(E) \exp(-E/k_B T)/Z$ with $Z = \sum_E g(E) \exp(-E/k_B T)$ can be calculated. $U(T)$ (blue and red curve) is invariant with respect to the normalization, whereas $F(T)$ differs for different normalizations by the term cT (c =constant). Assuming that c can be chosen (implying the use of another normalization), the $F(T)$ can be shifted until it matches with $U(T)$ at low temperature (yellow curve). Considering the yellow and the blue/red curve, the splitting point indicates an increase of entropy of the system ($S = (U - F)/T$), and thus, represents the transition temperature, similar as it was reported for the Al-Na alloy in Ref. [56].

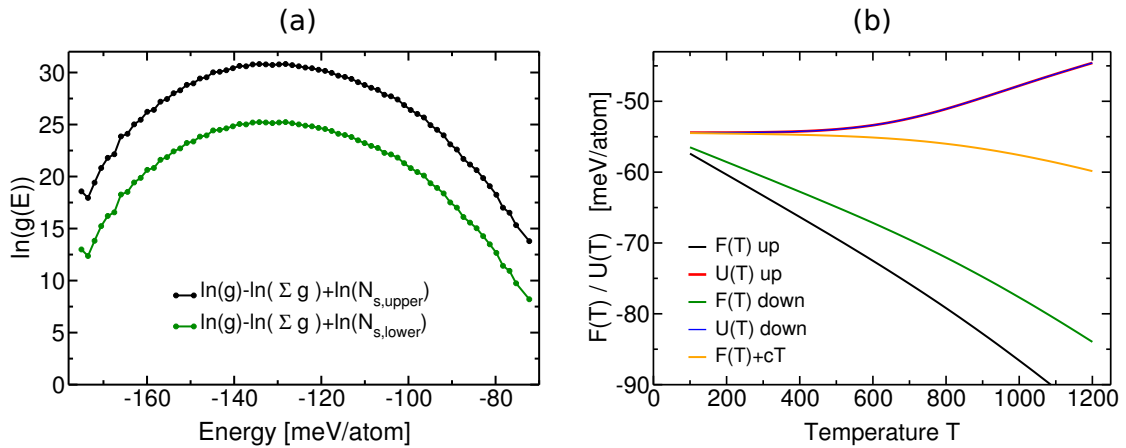


Figure B.2: (a) First test of the WL method for $\text{Ba}_8\text{Al}_x\text{Si}_{46-x}$ with $x = 11$. The final modification factor is 1.0001. (b) Free energy $F(T)$ and internal energy $U(T)$.

B.3 Compressive sensing

The plot depicts an example of the CS performed with LASSO. Here, the CV and the MSE vs. the sparsity μ shows a similar behavior as the CV for different set of clusters (see Fig. 6.1). A large μ leads to a small set of clusters and vice versa. For a small μ , many clusters are selected and result in an overfitting. The optimal μ , that leads to the optimal set of clusters, is indicated by the CV minimum.

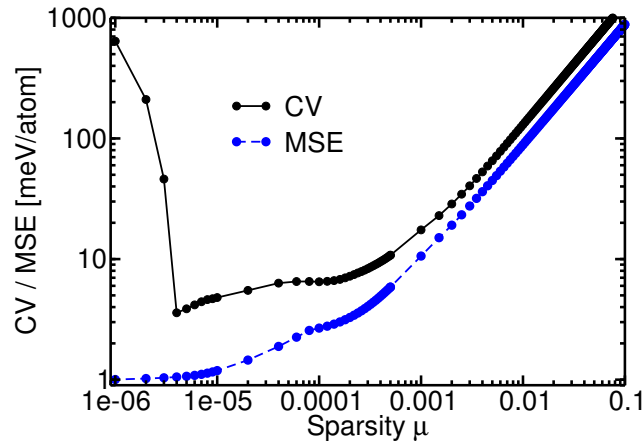


Figure B.3: Example of CS with LASSO.

Abbreviations

Acronym	Designation
<i>a.i.</i>	<i>ab-initio</i>
BM	Birch-Murnaghan
DOS	Density of states
CE	Cluster expansion
CS	Compressive sensing
CV	Cross validation
CDOS	Configurational density of states
DOS	Density of states
DFT	Density functional theory
F	Fermi
FLOP	Floating point operation per second
GS	Ground state
GSS	ground state search
LASSO	Least absolute shrinkage and selection operator
MS	Metropolis sampling
MSE	Mean square error
MT	Muffin-tin
OF	Occupancy factor
SCF	Self-consistent field

Acknowledgement

I would like to acknowledge the exceptional supervision, technical knowledge and moral support of my supervisor Claudia Draxl, head of the research group “Theoretische Festkörperphysik”.

My special gratitude to my mentor, Santiago Rigamonti, who encouraged me with his knowledge and experience, his steadfast support and inspiration have been invaluable during the work. Many thanks to all colleagues of Claudia’s group for instructive discussions and great collaboration. I am especially grateful to Pasquale Pavone for his interest, spirit and appropriate ideas to solve challenging topics.

I would like to extend my gratitude to our collaborators, the group of Yuri Grin (MPI, Dresden) and the group of Matthias Scheffler (FHI, Berlin), for insightful meetings widening the scope of my work.

Finally, I would like to thank friends and family, especially my partner Stephan and my mother Ute, for their patience and assistance in every situation.

Selbständigkeitserklärung

Hiermit versichere ich, dass ich die vorliegende Arbeit selbständig verfasst und keine anderen als die angegebenen Quellen und Hilfsmittel verwendet habe.

Berlin, den 18.12.2015

Unterschrift